


2015

Investigating the use of in situ liquid cell scanning transmission electron microscopy to explore DNA-mediated gold nanoparticle growth

Amanda Nguy
Iowa State University

Follow this and additional works at: <https://lib.dr.iastate.edu/etd>

 Part of the [Materials Science and Engineering Commons](#), and the [Mechanics of Materials Commons](#)

Recommended Citation

Nguy, Amanda, "Investigating the use of in situ liquid cell scanning transmission electron microscopy to explore DNA-mediated gold nanoparticle growth" (2015). *Graduate Theses and Dissertations*. 14930.
<https://lib.dr.iastate.edu/etd/14930>

This Thesis is brought to you for free and open access by the Iowa State University Capstones, Theses and Dissertations at Iowa State University Digital Repository. It has been accepted for inclusion in Graduate Theses and Dissertations by an authorized administrator of Iowa State University Digital Repository. For more information, please contact digirep@iastate.edu.

**Investigating the use of *in situ* liquid cell scanning transmission electron microscopy
to explore DNA-mediated gold nanoparticle growth**

by

Amanda Nguy

A thesis submitted to the graduate faculty
in partial fulfillment of the requirements for the degree of
MASTER OF SCIENCE

Major: Chemistry (Analytical)

Program of Study Committee:
Javier Vela, Major Professor
Emily Smith
Marit Nilsen-Hamilton

Iowa State University

Ames, Iowa

2015

Copyright © Amanda Nguy, 2015. All rights reserved.

TABLE OF CONTENTS

	Page
NOMENCLATURE	iv
ACKNOWLEDGMENTS	v
ABSTRACT	vii
CHAPTER 1 INTRODUCTION	1
The Importance of Understanding Growth Dynamics of Nanoparticles	1
Gold anisotropic nanoparticles	1
Changing gold nanoparticle morphologies	4
DNA as a template for gold nanoparticle growth	5
Non-thiolated, single-stranded DNA and DNA-mediated gold nanoparticle growth.....	9
Using the Liquid Cell for <i>In Situ</i> STEM Microscopy	12
<i>In situ</i> liquid phase scanning transmission electron microscopy (STEM).....	12
The liquid cell in STEM imaging.....	14
Differentiating between heterogeneous and homogeneous nucleation.....	16
CHAPTER 2 INVESTIGATING THE USE OF <i>IN SITU</i> STEM IMAGING TO EXPLORE DNA-MEDIATED GOLD NANOPARTICLE GROWTH.....	17
Introduction.....	17
Experimental Procedures	19
Synthesis of DNA-coated gold nanoprisms.....	19
Gold seed synthesis.....	20
Gold nanoprism formation.....	20
Etching of gold nanoprisms	22
DNA binding to gold nanoprisms.....	22
<i>Ex situ</i> experimental procedure.....	23
<i>In situ</i> experimental procedure.....	23
STEM imaging equipment and parameters.....	24
The liquid cell and the liquid cell holder	25
Results and Discussion	28
<i>Ex situ</i> results	28
<i>In situ</i> experiments.....	34
Fluid line set up and flow rate	34
Alternating reagent addition	39

Effect of liquid cell volume on flow and liquid cell environment.....	41
Conclusion.....	42
CHAPTER 3 COMPARING THE BINDING OF T30 AND A30 DNA TO GOLD NANOPARTICLES.....	45
Introduction	45
Experimental Procedures	48
~9 nM citrate-capped gold nanoparticle synthesis.....	48
Zeta potential measurements.....	49
Flocculation tests using absorption spectroscopy	49
Isothermal titration calorimetry (ITC)	49
Results and Discussion	50
Zeta potential measurements.....	50
Flocculation tests using absorption spectroscopy.....	51
Isothermal titration calorimetry (ITC) experiment to obtain binding enthalpy data.....	56
Conclusion and Future Directions	59
REFERENCES	62

NOMENCLATURE

AuNP	gold nanoparticle
LSPR	localized surface plasmon resonance
CTAB	cetyltrimethylammonium bromide
ssDNA	single-stranded DNA
dsDNA	double-stranded DNA
T30	30-base thymine oligonucleotide
A30	30-base adenosine oligonucleotide
Au-DNA NPrism	DNA-coated gold nanoprism
Au-T30 NPrism	T30-coated gold nanoprism
TEM	transmission electron microscopy
STEM	scanning transmission electron microscopy
HAADF	high-angle annular dark field
ITC	isothermal titration calorimetry

ACKNOWLEDGMENTS

Many, many thanks to Dr. Javier Vela for your continuous patience and support and without whom I would not have had the opportunity to finish my graduate work. I could not have gotten to this point without your guidance and positive attitude after a project change, a major professor change, and all the bumps in the road that went along with those events. Nothing could keep you from believing I could and should get to the finish line.

Emily Smith, I will forever appreciate all that you have done both in the roles as a committee member and as the DOGE throughout my career at ISU. Your patience and understanding will never be forgotten, and I promise I always took your invaluable advice to heart.

Very grateful thank yous to Tanya Prozorov and Taylor Woehl for letting me work on a fascinating project using cutting edge techniques. Tanya, although research can be very discouraging at times, I will never forget your unparalleled enthusiasm and encouragement to remind me that I can and will get to where I want to be. Taylor, thanks for putting up with me hovering over your shoulder in an attempt to soak up all your invaluable knowledge in a very short period of time.

Thanks to Dr. Ning Fang for the guidance you provided at the beginning of my career at ISU and understanding what I wanted my educational priorities to be.

Finally, thanks to all my friends, family, and loved ones for their unconditional support and love.

T.P. acknowledges support from the Department of Energy Office of Science Early Career Research Award, Biomolecular Materials Program. This work was supported by the U.S. Department of Energy, Office of Basic Energy Science, Division of Materials Sciences and Engineering. The research was performed at the Ames Laboratory, which is operated for the U.S. Department of Energy by Iowa State University under Contract No. DE-AC02-07CH11358.

ABSTRACT

Engineering nanoparticles with desired shape-dependent properties is the key to many applications in nanotechnology. Although many synthetic procedures exist to produce anisotropic gold nanoparticles, the dynamics of growth are typically unknown or hypothetical. In the case of seed-mediated growth in the presence of DNA into anisotropic nanoparticles, it is not known exactly how DNA directs growth into specific morphologies. A series of preliminary experiments were carried out to contribute to the investigation of the possible mechanism of DNA-mediated growth of gold nanoprisms into gold nanostars using liquid cell scanning transmission electron microscopy (STEM). Imaging in the liquid phase was achieved through the use of a liquid cell platform and liquid cell holder that allow the sample to be contained within a “chip sandwich” between two electron transparent windows. *Ex situ* growth experiments were performed using Au-T30 NPrisms (30-base thymine oligonucleotide-coated gold nanoprisms) that are expected to grow into gold nanostars. Growth to form these nanostars were imaged using TEM (transmission electron microscopy) and liquid cell STEM (scanning transmission electron microscopy).

An attempt to perform *in situ* growth experiments with the same Au-T30 nanoprisms revealed challenges in obtaining desired morphology results due to the environmental differences within the liquid cell compared to the *ex situ* environment. Different parameters in the experimental method were explored including fluid line set up, simultaneous and alternating reagent addition, and the effect of different liquid cell volumes to ensure adequate flow of reagents into the liquid cell.

Lastly, the binding affinities were compared for T30 and A30 DNA incubated with gold nanoparticles using zeta potential measurements, absorption spectroscopy, and isothermal titration calorimetry (ITC). It was previously reported thymine bases have a lower binding affinity to gold surfaces than adenine bases. However, the results reported here contradict the previously reported data. Future perspectives on this work are outlined.

CHAPTER 1

INTRODUCTION

The Importance of Understanding Growth Dynamics of Nanoparticles

Gold anisotropic nanoparticles

When metal particles reach dimensions of the nanometer scale they take on properties in great contrast to those of their bulk material. For example, a noble metal such as gold, in bulk, is relatively unreactive, but when it is 10 nm or smaller gold can become a catalyst^{1,2}. Specifically, gold nanoparticles (AuNPs) are of great interest because of their unique electronic and optical properties^{3,4}, which are useful for applications in areas such as sensing^{5,6}, imaging⁷, and catalysis⁸. Such properties can be tuned in the visible and near IR regions of the electromagnetic spectrum by controlling different factors such as size and shape^{9,10,11}. The benefit of these properties is exhibited through the presence of localized surface plasmon resonance (LSPR) which is produced when light hits a metal nanoparticle (Figure 1). LSPRs are free oscillating electrons that resonate with the oscillations of the electromagnetic field, creating a strong absorption band.

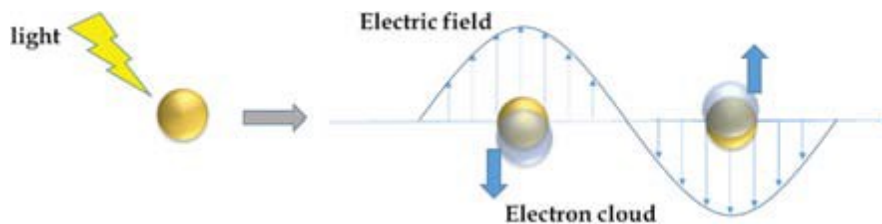


Figure 1 Diagram of localized surface plasmon resonance of a metal nanoparticle¹⁹. Reprinted with permission from [19] Alex, S.; Tiwari, A. *J. Nanosci. and Nanotechnol.* **2015**, *15*, 1869-1894. Copyright 2015, American Scientific Publishers

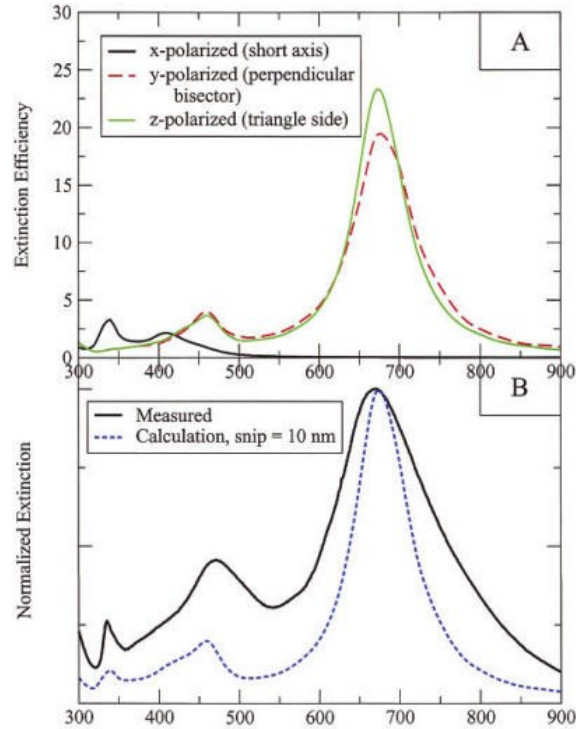


Figure 2 Absorption spectra of trigonal Ag prisms with side length = 100 nm and thickness = 16 nm. A) Calculated spectra for polarization along the three primary axes. B) Average over orientation, along with measured spectrum¹⁰. Reprinted with permission from [10] Kelly, K. L.; Coronado, E.; Zhao, L. L.; Schatz, G. C. *J. Phys. Chem. B* **2003**, *107*, 668-677. Copyright 2003, American Chemical Society.

The shapes of AuNPs have been shown to enhance these optical properties compared to spherical, non-hollow AuNPs¹² due to the fact that these anisotropic nanoparticles can have multiple surface plasmon resonances depending on the size and shape. For example, it was shown that 100-nm silver nanotriangles have two LSPR peaks at 460 nm and 670 nm (Figure 2)¹⁰.

Figure 3a shows where increased electrical fields reside on the nanoprism compared to silver nanospheres (Figure 3b). It can be seen that there is significant

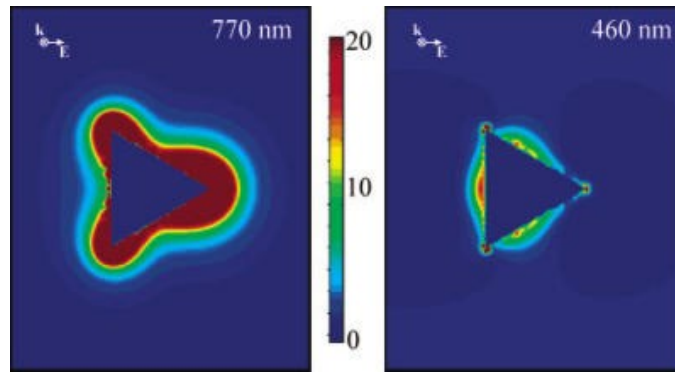


Figure 3a Electric field enhancement contours external to the Ag trigonal prism, for a plane that is perpendicular to the trigonal axis and that passes midway through the prism¹⁰. Reprinted with permission from [10] Kelly, K. L.; Coronado, E.; Zhao, L. L.; Schatz, G. C. *J. Phys. Chem. B* **2003**, *107*, 668-677. Copyright 2003, American Chemical Society.

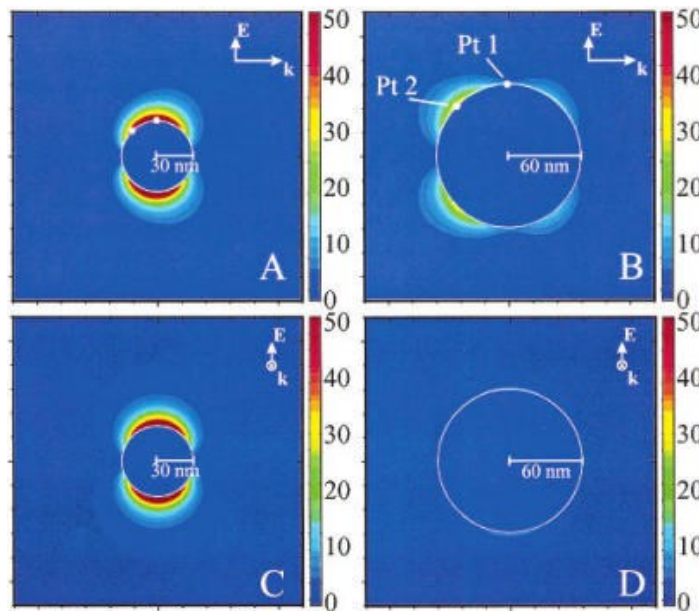


Figure 3b E-field contours for radius 30 and 60 nm Ag spheres in a vacuum. Two cross-sections are depicted for each sphere. (a,b) The plane containing the propagation and polarization axes and (c,d) the plane perpendicular to the propagation axis. The $r = 30$ nm sphere LSPR = 369 nm and the $r = 60$ nm sphere LSPR = 358 nm¹⁰. Reprinted with permission from [10] Kelly, K. L.; Coronado, E.; Zhao, L. L.; Schatz, G. C. *J. Phys. Chem. B* **2003**, *107*, 668-677. Copyright 2003, American Chemical Society.

enhancement at the points of the nanoprism for the 770 nm LSPR peak. Due to this major advantage in optical properties, emphasis has increased in the last decade on how to engineer AuNPs of specific shapes and morphologies reproducibly.

Changing gold nanoparticle morphologies

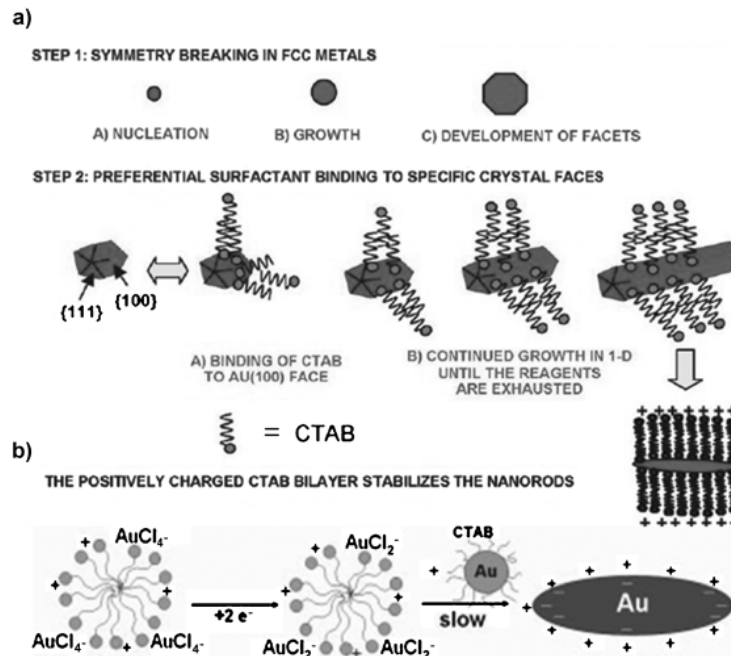


Figure 4 Mechanism for the formation of gold nanorods using CTAB as a growth template (a)⁴ Reprinted with permission from [4] Murphy, C. J.; Sau, T. K.; Gole, A. M.; Orendorff, C. J.; Gao, J.; Gou, L.; Hunyadi, S. E.; Li, T. *J. Phys. Chem. B* **2005**, *109*, 13857-13870. Copyright 2005, American Chemical Society. (b)⁶⁵ Reprinted with permission from [65] Perez-Juste, J.; Liz-Marzan, L. M.; Carnie, S.; Chan, D. Y. C.; Mulvaney, P. *Adv. Funct. Mat.* **2004**, *14*, 571-579. Copyright 2004, John Wiley and Sons.

Controlling the production of specific sizes and shapes of nanoparticles is essential to any application in nanotechnology. An abundance of shapes have been synthesized such as nanorods^{13, 14}, nanowires^{15, 16}, and nanoprisms^{17, 18}. The most common method to synthesize anisotropic nanoparticles is starting with the modern seed mediated method¹⁹. Although this gold seed synthesis is a well-known and robust technique in the world of synthesis, it is equally well known how difficult it can be to tune to a desired size and shape reproducibly after the formation of those seeds. The first non-spherical shape to be made was gold nanorods by the Murphy research group in which cetyltrimethylammonium bromide (CTAB) prevented gold (III) ion reduction onto

the {100} faces of gold seeds, thus facilitating extended growth on the {111} faces (Figure 4)¹³.

This is one of the basic principles for a number of procedures used for making nanoparticles grow into different shapes: organic molecules and other ligands are used to physically constrict growth to certain directions.

DNA as a template for gold nanoparticle growth

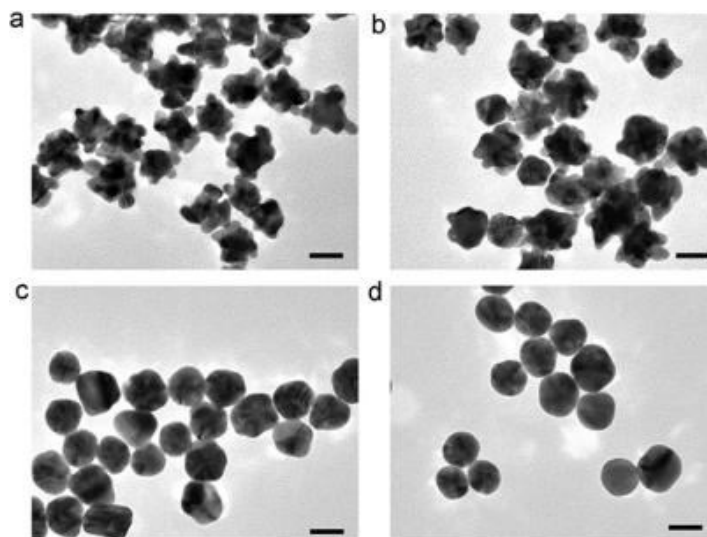


Figure 5 TEM images of gold nanoparticles prepared with a) A30, b) C30, c) T30, and d) absence of DNA. Scale bar: 20 nm²⁵. Reprinted with permission from [25] Wang, Z.; Zhang, J.; Ekman, J. M.; Kenis, P. J. A.; Lu, Y. *Nano Lett.* **2010**, *10*, 1886-1891. Copyright 2010, American Chemical Society.

Today, DNA is a popular choice for use as a template when making nanoparticles of different morphologies. However, it is not known exactly how DNA mediates growth into different shapes. In 1996, thiolated DNA was used to functionalize gold nanoparticles for the first time, but they were used to assemble macroscale structures in which complementary bases would pair with each other^{20, 21}. For morphological change of a single nanoparticle, the dynamics for growth are not known when DNA is used as

the growth template. It is well known that the thiolated ends of single stranded DNA will covalently bind to the surface of a gold nanoparticle^{22, 23, 24} and the nitrogen in the bases of the DNA could interact with the particle surface²⁴ as well, but the route through which anisotropic gold nanoparticles grow into specific shapes remains a mystery. It was demonstrated for the first time that single-stranded DNA (ssDNA) adsorbed onto a nanoparticle surface could direct growth into different morphologies (Figure 5)²⁵. The oligonucleotides were 30 repeating bases of thymine (T), adenine (A), or cytosine (C). The work presented in this thesis focuses on thymine and adenine (Figure 6).

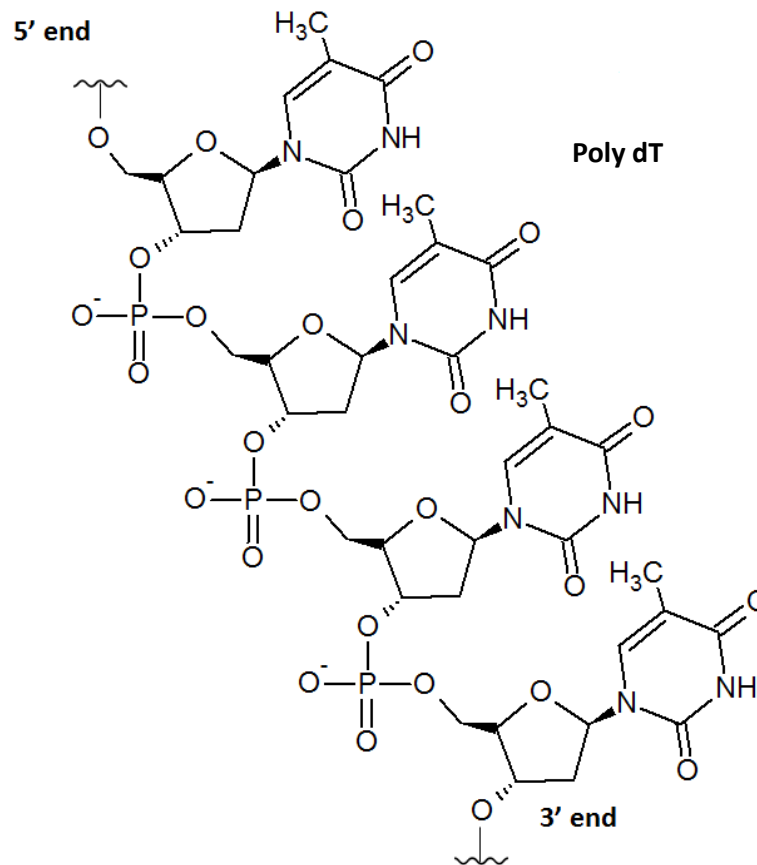


Figure 6a Molecular structure of single stranded thymine oligonucleotide DNA. T30 would have 30 repeating thymine bases and the 5' and 3' ends would be terminated with an –OH group.

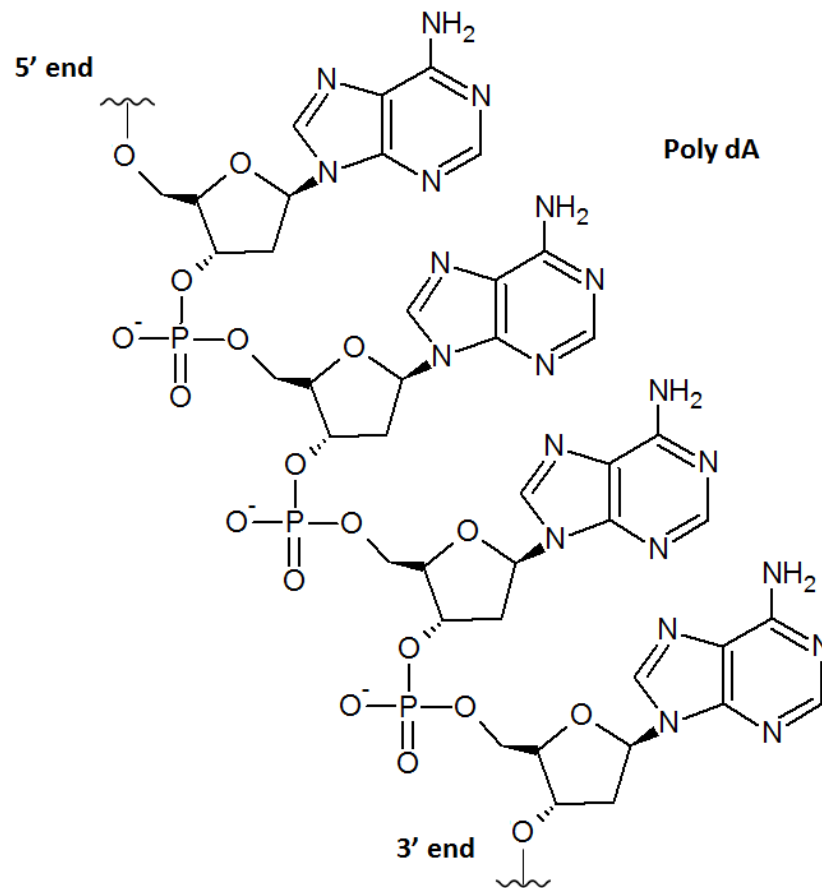


Figure 6b Molecular structure of single stranded adenine oligonucleotide DNA. A30 would have 30 repeating adenine bases and the 5' and 3' ends would be terminated with an –OH group.

Interestingly, the same DNA oligonucleotides form even more interesting shapes when bound to gold nanoprisms. In this work by Wang et al., oligonucleotides with 30 repeating bases of adenine, thymine, cytosine, and nanoprisms with 20 bases of guanine were explored (Figure 7)²⁶.

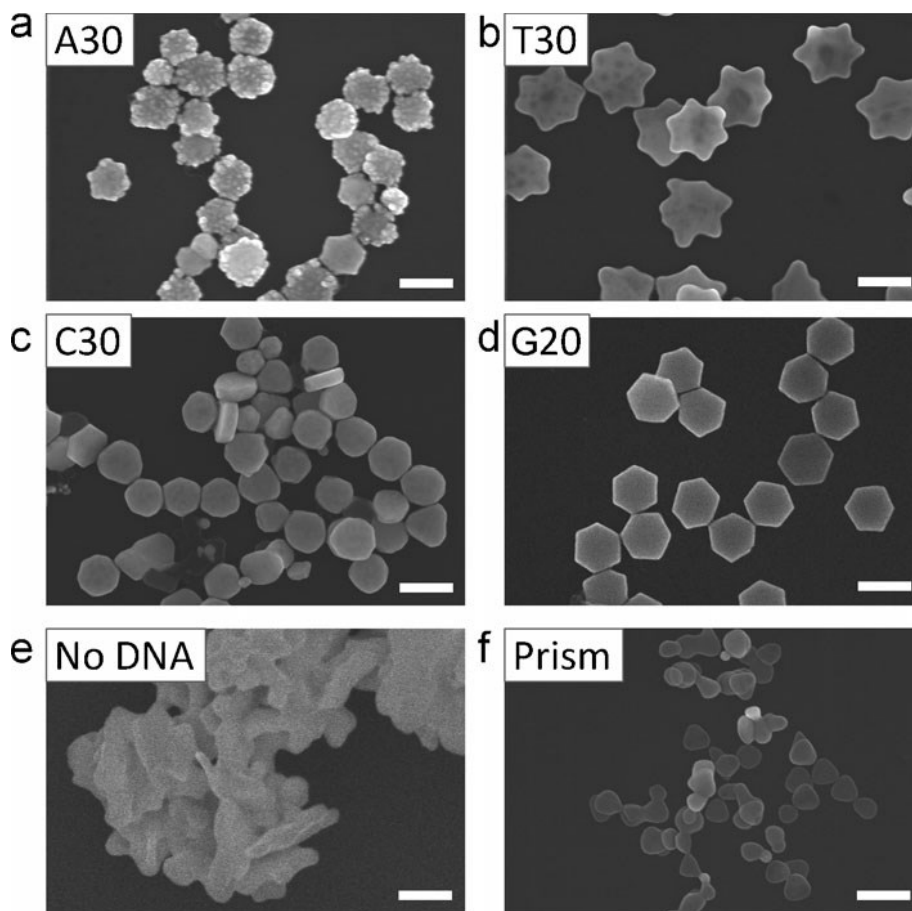


Figure 7 SEM images of gold nanoprisms prepared with a) A30, b) T30, c) C30, d) G30, e) absence of DNA, and f) absence of gold salt. Scale bar: 200 nm²⁶. Reprinted with permission from [26] Wang, Z.; Tang, L.; Tan, L. H.; Li, J.; Lu, Y. *Angew. Chem.* **2012**, *124*, 9212-9216. Copyright 2012, John Wiley Sons.

Non-thiolated, single-stranded DNA and DNA-mediated gold nanoparticle growth

Non-thiolated, single-stranded DNA oligonucleotides incubated with the aforementioned nanoprisms are directing growth from the ions reduced in solution. However, it is not certain what drives the ions to be reduced onto which surfaces of the nanoprisms. The mystery of the role of DNA in this process stems from the fact that it is not certain through which mechanism or mechanisms non-thiolated, single-stranded oligonucleotides bind with gold nanoparticles. There are multiple sources of interactions including electrostatic interactions, forces due to the hydrophobic effect, and nonspecific

chemical bonding through the exposed bases²⁷, but the specific contributions and interplay of these interactions are unknown²⁸.

In the case of electrostatic interactions, ssDNA is able to uncoil and expose the DNA bases. This flexibility in orientation and configuration affects the repulsion of the negatively charged phosphate backbone by the negatively charged, citrate-capped nanoparticle surface and exposes the DNA bases, which in turn allow gold-DNA base van der Waals interactions to occur^{29,30}. In contrast, double-stranded DNA (dsDNA) exists as a stable double-helix, keeping the bases on the inside of the double-helix while the phosphate backbone stays on the outside allowing repulsion by gold nanoparticle surfaces. Consequently, dsDNA does not appreciably adsorb onto gold nanoparticle surfaces³¹.

The conformation of DNA is also affected by the hydrophobic effect which occurs when a large molecule with hydrophobic regions changes its configuration to minimize the exposure of these areas to water molecules. ssDNA has exposed hydrophobic bases, so it will coil upon dehydration of the bases. Thus, hydrophobicity of the DNA bases affect the conformation of the molecule³². Reports suggest that adenine bases are less likely to be dehydrated than thymine bases since they can bind to five water molecules due to the aromatic nitrogen atoms, the N1 nitrogen atom, and amine group of adenine. Thymine, in comparison, can only bind three water molecules at the two carbonyl oxygen atoms and at the imine (NH) site (Figure 8)³³. Consequently, thymine is more likely to coil than adenine.

Finally, there is specific bonding between the DNA bases and gold nanoparticle surfaces due to physisorption^{34,35} and chemisorption³⁶. Adenine bases are reported to bind by way of a coordination mechanism involving the nitrogen atom of the imidazole ring and the C-NH₂ group whereas thymine binds by way of the oxygen of the C4 carbonyl group (Figure 8).

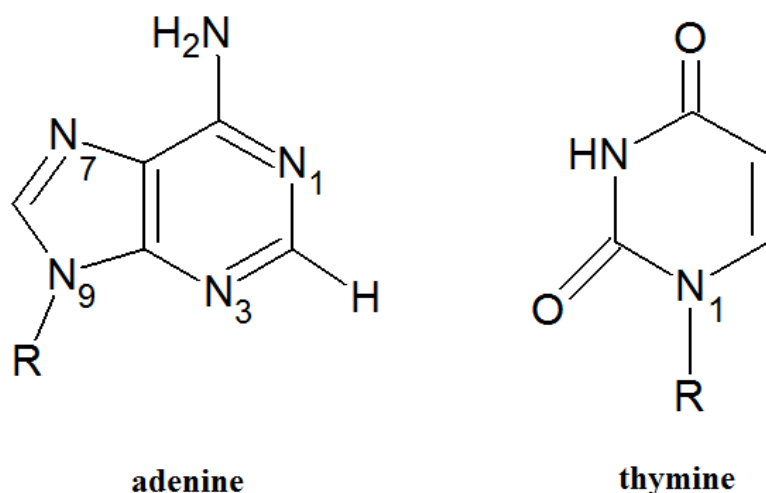


Figure 8 Molecular structures of the nucleotides adenine (left) and thymine (right)..

If we reflect on the previously mentioned theories on how anisotropic nanoparticles are created, the DNA serves as a template where the ions are reduced along the DNA which acts like a supporting scaffold, or the DNA restricts growth by confinement in some areas but not in others causing accumulation in unrestricted areas. Since the majority of the interactions are between the DNA bases and the gold nanoparticle surface, we focus on conformations of DNA which assume the phosphate backbone has less significant interactions. With these ideas in mind, we attempted to reveal more about the mechanism of gold nanoprism growth by capturing images using scanning transmission electron microscopy (STEM) in the liquid phase.

Using the Liquid Cell for *In Situ* STEM Microscopy

In situ liquid phase scanning transmission electron microscopy (STEM)

With the development of the liquid cell for STEM microscopy, there have been many new reports regarding nanoparticle growth. They include work on direct observation studies³⁷⁻³⁸, aggregation^{39,40,38,41,42}, and coalescence^{37,43,44}. The liquid cell enables STEM imaging of liquid samples by enclosing them in a cell that can be set into a holder which goes into the vacuum column, as is usual in electron microscopy. This allows for imaging of nanoparticle growth almost in real time as ions are reduced in solution to create nucleation. It is unclear whether this nucleation is via the classical nucleation theory or via pre-nucleation clusters as described by non-classical nucleation theory⁴⁵. The principles of imaging are the same for STEM not in the liquid phase. The image is constructed using electrons which have been transmitted by an electron transparent sample. A field emission gun (FEG) provides the finite-sized electron source beam which is de-magnified by an electromagnetic condenser lens to form the probe. The probe size is restricted by a condenser lens aperture, scanned in a raster over the sample, and the signals are detected and plotted as a function of probe position. There are multiple signals that can be detected in STEM imaging.

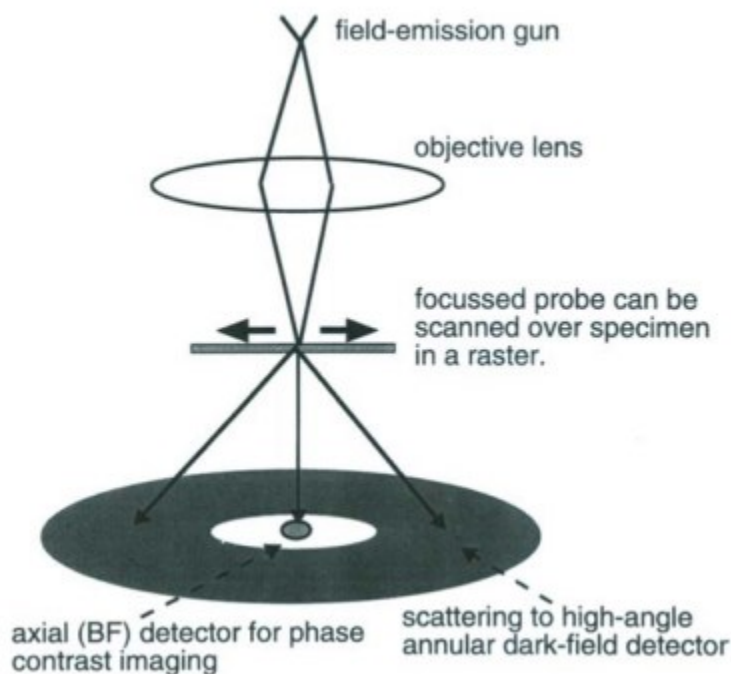


Figure 9 General optics layout of a TEM/STEM microscope⁶⁹. Reprinted with permission from [67] Nellist, P. D.; Pennycook, S. J. *Advances in Imaging and Electron Physics* **2000**, *123*, 173-206. Copyright 2000, Elsevier B.V.

In liquid cell STEM, electrons are transmitted by a thin sample, ideally around 100-200 nm thick. Coherent and incoherent elastically scattered electrons, inelastically scattered electrons, backscattered electrons, and/or secondary electrons can be collected. For the images taken in this work, we focus on elastically electrons scattered at high angles with respect to the optical axis. These Rutherford scattered electrons are collected by a high angle annular dark field (HAADF) detector. Since Rutherford scattering is produced by coulombic interactions with nuclei rather than electron clouds, the image obtained has intensities represented by $I \propto tZ^2$, where Z is the atomic number of the metal being imaged and t is the thickness. This allows us to discern whether the nanoparticles are composed of the same metal.

The liquid cell in STEM imaging

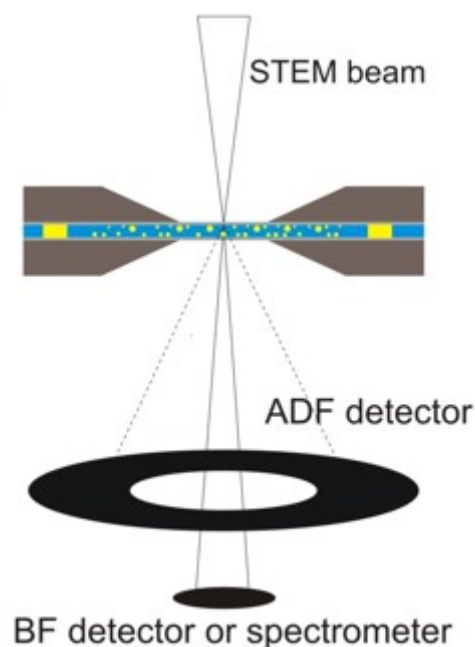


Figure 10 Diagram of the liquid cell provides a pathway for electrons to travel through an electron transparent window and to the detector. Diagram by Taylor Woehl.

The liquid cell is composed to two thin silicon wafers with silicon nitride windows etched out of the center. The windows are electron transparent, allowing the sample to stay in the liquid phase, but electrons can still be transmitted (Figure 10). Additionally, the liquid cell holder used in these experiments is a continuous fluid flow holder, allowing *in situ* addition of reagents which can be flowed into the liquid cell in real time. This creates the capability to witness growth almost in real time, as if one could be a nanofly on the wall off a synthetic reaction vessel. The microfluidic lines are externally accessible on the liquid cell holder, so one can inject reagents in one line and the excess liquid in the cell is pushed out the other line. This theoretically gives rise to the

possibility of continuous flow of the liquid environment and controlled addition of desired reagents.

Although the principles of imaging are the same whether or not in the liquid phase, there are additional artifacts that can affect imaging when using the liquid cell holder. Regarding assembly of the “chip sandwich” that comprises the liquid cell, it must be enclosed in the liquid cell holder and then put in a vacuum. When put under very low pressures, the windows bulge outward, causing bubbles to form^{46, 47, 48} and a decrease of resolution due to a thicker liquid layer⁴⁸. If this occurs, one can adjust the window geometry to try to reduce the window bulge. It is important to use a liquid cell with a spacer chip large enough to provide an adequate liquid layer, but small enough that you have adequate spatial resolution. The thickness of the liquid layer not only creates a wide physical barrier through which electrons must travel, but more liquid means more radiolysis of water. It is known that irradiating water with electrons in STEM imaging creates hydrogen radicals and aqueous electrons, which are both strong reducing agents⁴⁹. This is a nuisance since it can at times be hard to discern whether or not growth of nanoparticles is due to chemical reduction. Ions in solution reduced by the large numbers of electrons supplied by the electron beam tend to nucleate homogeneously. In order to minimize unnecessary electron beam reduction, the beam can be blanked when images are not being acquired.

Additionally, the liquid layer can evaporate when put under the vacuum. This is due to incomplete vacuum sealing probably due to dirt or dust on the rubber o-rings of the fluid stage holder. A few gentle spurts from a compressed air can help with the assembly of a well-sealed chip sandwich. During sample preparation, take care to make

sure there is no carbon contamination on the chips. Chips should be cleaned using an ozone/UV plasma cleaner. Finally, there can be some artifacts caused by electron beam-sample interactions. One may see growth of nanocrystals outside of the irradiated area. To remedy this issue, be sure to image below the electron dose rate threshold. This will also help to prevent unnecessary charging of the windows and particles by the electron beam ⁴².

Differentiating between homogeneous and heterogeneous nucleation

The key to successful gold nanoparticle growth in the liquid cell is overcoming the preference for ions in solution to nucleate homogeneously. In homogeneous nucleation, small particles nucleate out of solution with no initial substrate. In order for nanoparticles to change from one shape to another, there must be heterogeneous nucleation, in which the nanoprisms are used as the growth substrate. Structures of different nanocrystals have stacking faults and/or twin planes that serve as nucleation sites that should promote growth in specific directions. It is important to choose a template nanoparticle with such features. An ideal successful morphology change experiment would show the change from the initial template shape to the desired shape without any growth of nucleated particles in the surrounding solution. Since homogeneous nucleation is significantly initiated by electron beam reduction, it is imperative that the beam dosage is reduced or the beam is blanked as much as possible between successive image acquisitions.

CHAPTER 2

INVESTIGATING THE USE OF IN SITU LIQUID CELL STEM TO EXPLORE THE DYNAMICS OF DNA MEDIATED GOLD NANOPARTICLE GROWTH

Introduction

It was previously reported that gold nanoprisms changed from triangular prisms to 6-pointed stars and in the presence of gold (III) ion and reductant when incubated with 30-base thymine (T30) or 30-base adenine (A30) oligonucleotide, respectively (Figures 7a and 7b)²⁶. However, the mechanism of how growth proceeds is not known. It would be beneficial to see how the growth progresses in order to gain insight into how to specifically engineer the syntheses of these particles. This work will focus on T30 and will start with replication of the nanoprisms used in the literature, replication of the morphology change experiments *ex situ*, further exploration of the growth mechanism *in situ*, and consequently, some optimization steps that were taken for the *in situ* experiments.

Seed-mediated synthesis methods are commonly reported for use in making nanoparticles with specific morphologies¹⁹. A synthesis procedure using iodide ion to facilitate nanoprism formation⁵⁰ was adapted. Gold nanoprisms are twinned and planar with {111} facets on the flat top and bottom surfaces and stacking faults in the vertical direction on the side faces^{51, 52, 53}. It is shown that the iodide ion preferentially binds to the {111} facets of gold, and it is surmised that this contributes to the preferential creation of a surfactant bilayer at the other crystal facets⁵⁰. The cationic surfactant used in this synthesis method, cetyltrimethylammonium bromide (CTAB), can form layers that

prevent gold reduction at those other facets⁵⁴. The twin plane and stacking faults are reported to facilitate preferred growth in the lateral direction along the twin defects and stacking faults^{6, 55, 56}. Due to these crystallographic features, we used these gold nanoprisms as our beginning template to monitor DNA-mediated growth. One would not get the same kind of preferential growth in certain directions if isotropic nanoparticles were used due to lack of stacking faults and twin planes.

As mentioned previously, the binding interactions of non-thiolated, single-stranded DNA are not certainly known. It is known, however, that certain DNA bases seem to have higher affinity to gold surfaces compared to others. For example, thymine has been reported to have the weakest binding affinity out of all the bases⁵⁷. Given that DNA is negatively charged, wherever there are capping ligands that provide for more positive surface charges are probably more preferred for electrostatic interactions. Since DNA bases are hydrophobic, if the gold nanoparticle surface is sufficiently hydrophobic, there may be hydrophobic effect interactions. Finally, there may be certain chemical interactions between certain atoms on the DNA bases and the gold nanoparticle surfaces. Whether the sites with DNA adsorption prevent or promote sites for ion reduction is unknown. These interactions are what determine the change in morphology of the nanoprisms.

The nanoprisms were incubated with T30, which are single stranded oligonucleotides with repeating thymine bases. These gold nanoprisms with bound T30 DNA (Au-T30 NPrisms) were used in all growth experiments.

Experimental Procedures

Synthesis of DNA coated nanoprisms

Au-T30 NPrisms were prepared using the following steps: gold seed synthesis, nanoprism formation, a dilution procedure which etches the corners of the nanoprisms, and an incubation period with 30-base oligonucleotides. Figure 11a shows the distribution for diameter of the nanoprisms. Most of the nanoprisms were around 110 nm.

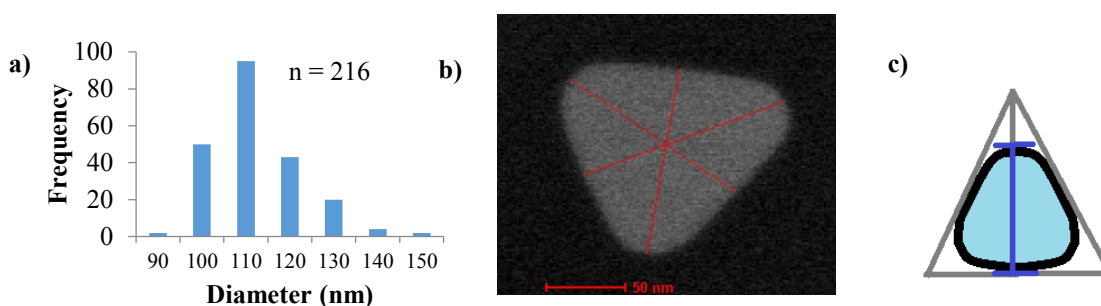


Figure 11 a) Distribution of diameters for Au-T30 nanoprisms, n = 216. b) Au-DNA nanoprisms with red lines showing how diameter measurements were taken. c) Simplified diagram showing how diameter measurements were taken from the bisection of a rounded corner to the opposite side.

Solutions were made the day of synthesis except for the 100 mM sodium hydroxide solution, which was kept as a stock solution. All water used is 18.2 MΩ (MΩ) Milli-Q water, all glassware was thoroughly cleaned using 2.5 M sodium hydroxide and aqua regia composed of 3 parts hydrochloric acid and 1 part nitric acid (CAUTION: Aqua regia is a powerful oxidizing agent and it should be handled with extreme care!), with water rinses in between each stage. Oligo dT₃₀ and oligo dA₃₀ were purchased from Integrated DNA Technologies (Coralville, IA). Hydrogen tetrachloroaurate (III) hydrate (HAuCl₄·3H₂O, 99.999%), hydroxylamine hydrochloride (NH₂OH·HCl, 99.9999%), cetyltrimethylammonium bromide (CTAB), trisodium citrate

(99%) L-ascorbic acid (99%), sodium borohydride (NaBH_4 , 99.995%) and sodium iodide (98%) were purchased from Sigma-Aldrich. All chemicals were used as received.

Gold seed synthesis

To prepare gold seeds, gold ions from a 10mM gold stock solution were reduced by 100mM sodium borohydride. The gold stock solution was made by dissolving 16 mg of $\text{HAuCl}_4 \cdot 3\text{H}_2\text{O}$ in 4 mL of water. A 10 mM citrate solution was made by dissolving 2.58 mg of sodium citrate in 1 mL of water. To a round bottom flask 36 mL of water, 1 mL of the 10 mM citrate solution and 1 mL of the gold stock solution were added and set to stir at 600 rpm. 3.78 mg sodium borohydride was added to 1 mL water to make a 100 mM solution, which was all added to the mixture in the round bottom flask, changing the color of the mixture from pale yellow to a dark red wine color immediately upon sodium borohydride addition. This mixture was stirred for exactly one minute, then left to age for at least 2 hours.

Gold nanoprism formation

The cationic surfactant cetyltrimethylammonium bromide (CTAB) and sodium iodide is used to facilitate growth of nanoprisms from the gold citrate seeds. A 50 mM CTAB solution was made by dissolving 2.73 g of CTAB in a 250 mL Erlenmeyer flask under constant stirring and gentle heating to assure complete dissolution. 100 mM

sodium iodide solution was made by dissolving 14.9 mg sodium iodide in 0.5 mL water. 75 μ L of this sodium iodide solution was added to the dissolved CTAB.

1 mL of 100 mM ascorbic acid was prepared by dissolving 17.6 mg L-ascorbic acid in 1 mL of water, and 100 mM sodium hydroxide was prepared by adding 40 mg sodium hydroxide to 10 mL water.

The ascorbic acid solution, sodium hydroxide solution, gold citrate seeds, CTAB-sodium iodide solution, and gold stock solution were used to make 3 growth solutions. Solutions A and B both contained 9 mL CTAB-sodium citrate solution, which was a colorless and clear solution in a 15 mL plastic centrifuge tube. The following procedure applies to Solutions A and B, only: addition of 250 μ L 10 mM gold stock solution turned the solution a yellow-orange color. 50 μ L of 100 mM sodium hydroxide was added and the yellow-orange color became lighter. Finally, 100 mM ascorbic acid turned the solution colorless again. Solution C contained all the same additions, but the volumes were 10 times the volumes used for Solutions A and B and contained in a 250 mL Erlenmeyer flask.

The following procedure was done only after gold seeds had aged for at least 2 hours: 1 mL of gold seeds was added to Solution A and pipetted up and down rapidly for mixing 7 or 8 times. 1 mL of this mixed solution was immediately added to Solution B, which was capped, shaken vigorously by hand to mix thoroughly, and immediately all of this solution was poured into the Erlenmeyer flask containing Solution C which was swirled a few times to mix. This final solution was set in a 25°C water bath for at least 8 hours, usually overnight, to allow nanoprisms to settle out of solution.

Etching of gold nanoprisms

After the growth solution had rested overnight, a ring of nanoprisms had settled to the bottom of the Erlenmeyer flask. The CTAB solution was decanted, and then as much of the remaining purple CTAB solution was removed via a pipette. 5.5 mL water was added to the flask and swirled, showing a green color characteristic of the presence of nanoprisms with sharp corners. 150 μ L aliquots of this green nanoprism solution was dispensed into 0.5 mL centrifuge tubes. The following steps were a purification process: Nanoprisms in all tubes were diluted with 200 μ L water, and centrifuged for 2 minutes at 6100g. The supernatant was removed using a micropipette, leaving the pellet of nanoprisms. 300 μ L of water was added to the nanoprisms and the centrifugation was repeated for another 2 minutes. The supernatant was once again removed and finally the purified nanoprisms were diluted with 100 μ L water and left to rest while the corners of the nanoprisms were etched into rounded corners. The solution changed from green to a turquoise color when the corners were round. It is possible the rounded corners provide a preferential surface for the DNA to bind due to the reduction of steric hindrance after as DNA is loaded onto the surface of the nanoprisms.

DNA binding to gold nanoprisms

10 μ L aliquots of the rounded nanoprisms were transferred to clean 0.35 mL centrifuge tubes. 2 μ L of thawed T30 was added, mixed, and the sample was left to incubate with the DNA for 15-30 minutes.

***Ex situ* experimental procedure**

Morphology change experiments were replicated *ex situ*. In these experiments, 2 μL Au-T30 NPrisms were allowed to react with 1 μL of 200 mM hydroxylamine (HA), and then 0.5 μL 0.8% (w/w) hydrogen tetrachloroaurate (III) hydrate in a centrifuge tube for at least 30 min. For TEM images, the sample was dropped onto a grid and the dried as usual. For liquid cell STEM images, the sample was dropped onto the SiN window, the liquid cell was assembled, and then the sample was imaged with no further reagent addition. It should be noted that the fluid lines were filled and primed with water, which will inevitably be sucked into the fluid cell when put into the vacuum.

***In situ* experimental procedure**

After it was confirmed the Au-DNA NPrisms successfully changed into the desired 6-pointed star using T30, *in situ* experiments were performed. In these experiments, 0.75 μL Au-T30 NPrisms were drop casted onto the SiN window, the liquid cell was assembled, and the sample was inserted into the microscope. During imaging, the gold precursor and reductant were delivered into the liquid cell by way of the small fluid lines that run from a syringe to the liquid cell sample holder. The fluid lines had previously been primed with the reagents that were to be flowed into the cell. Concentrations of reagent solutions could be changed during imaging simply by switching out the solutions in the syringes. However, it should be noted that the diameter of the internal fluid lines leading to the liquid cell is 100 microns, while the external fluid lines used to send solutions to the liquid cell are 1/16" in diameter. These diameters are

small enough to limit the movement of the solutions by diffusion and so it is not known what the actual concentration of reagents delivered to the cell are.

STEM imaging equipment and parameters

An FEI (Hillsboro, OR) Tecnai 2-F20 STEM microscope with a Hummingbird Scientific (Lacey, WA) liquid cell sample holder was used to take all images. Electron dosage was minimized to reduce unnecessary electron beam reduction using a specific spot size, magnification, and dwell time. The spot size, a measure of the condenser aperture 1 (C1) magnetic lens crossover strength, was 8 at 56,000x-79,000x or 9 for 110,000x and above. For acquisition of images, magnification was generally 56,000x-79,000x with an 8 μ s dwell time. The electron dose was $3.27 \times 10^7 \text{ e}^-/\text{nm}^2$ and $4.18 \times 10^9 \text{ e}^-/\text{nm}^2$ for 56kx and 79kx, respectively. For a closer look at 2-5 nm nucleated particles, the magnification was increased to at least 320,000x, corresponding to an electron dose of $2.05 \times 10^{10} \text{ e}^-/\text{nm}^2$. The condenser aperture 2 (C2) setting was 70 μ m and the beam current was approximately 107 pA for spot size 8 and 30 pA for spot size 9. A camera length of 114 mm was used to limit background noise.

The liquid cell holder and the liquid cell

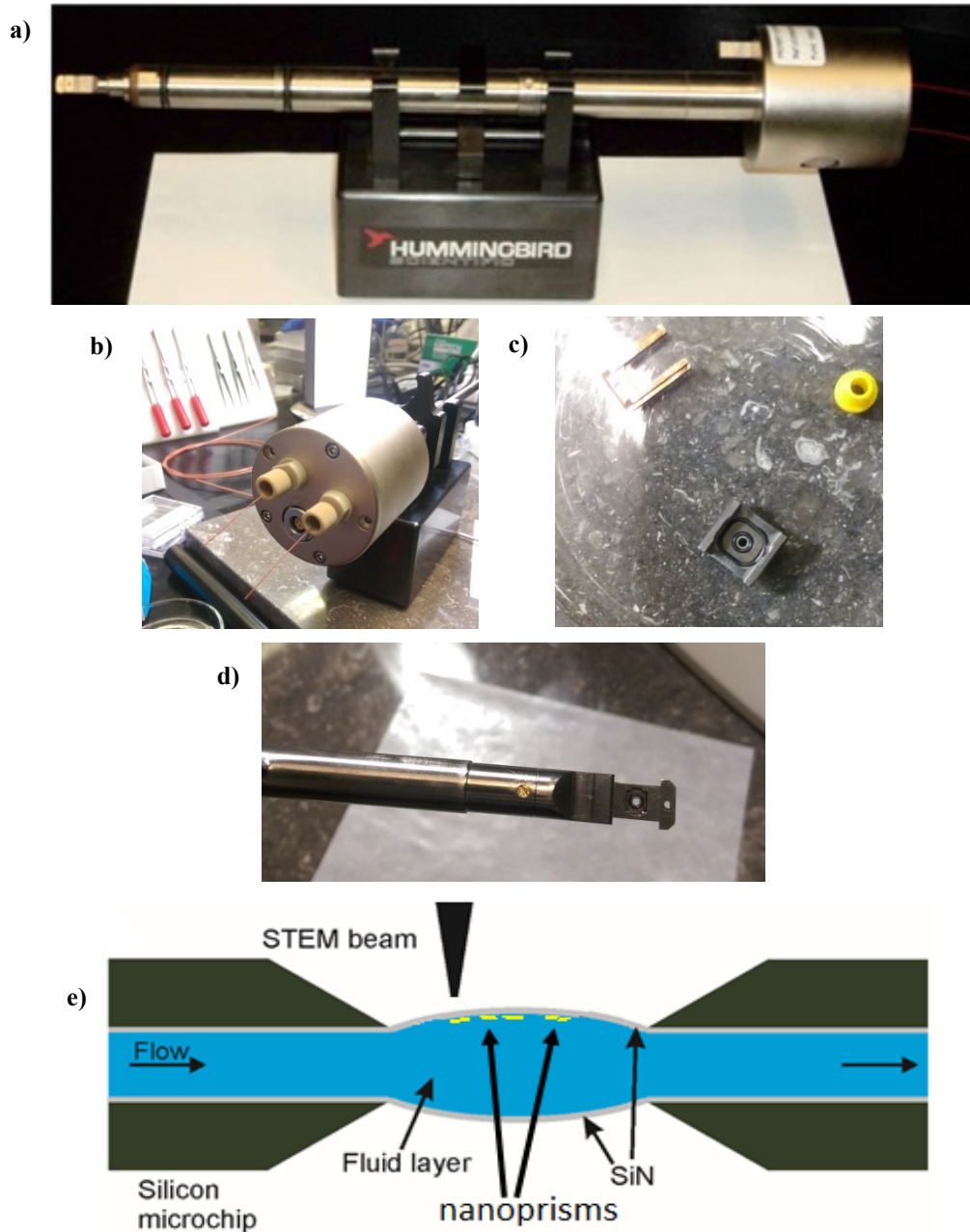


Figure 12 a) Exterior view of the Hummingbird Scientific liquid cell holder b) The back chamber of the liquid cell holder with the fluid lines protruding out the back. c) The cover for the tip (shown in part d) which seals the liquid cell, enabling it to be put in the vacuum column. d) A close up look at the tip which houses the “chip sandwich”. e) Simplified diagram of the silicon microchip “sandwich” showing the liquid flow through the cell and the slight bulge of the window under vacuum. Drawing by Taylor Woehl.

The main parts of the liquid cell holder are the tip where the sample is housed and from where small fluid lines originate (Figure 12d) and the back chamber where the bulk of the length of the fluid lines are housed (Figure 12b). The fluid lines can be externally accessed from this back chamber, where they can be connected to larger fluid lines which are used to flow reagents into the tip of the holder. A shaft through which the small fluid lines run connects the two parts and looks very similar to the shaft of a normal TEM grid sample holder (Figure 12a). The most critical part of the liquid cell holder is the tip and the tip cover (Figure 12c), which includes several rubber o-rings to ensure a vacuum seal around the “chip sandwich”. This “chip sandwich” acts as the liquid cell (Figure 12e).

The chips used in the “chip sandwich” are silicon wafers with a thin layer of electron-transparent silicon nitride on them. Sections are etched out of the silicon wafers, leaving 50 x 200 μm electron-transparent windows. Chips can be blank chips (without spacers) or have spacers with varying heights. One spacer chip in combination with a blank chip or a second spacer chip creates the liquid cell with varying volumes, depending on the combination of spacer height. When the chips are stacked together with the silicon nitride windows on the inside of the sandwich the windows are overlapped, forming an enclosed liquid cell with a window on the top and bottom. When under a vacuum, the windows bulge as liquid is drawn into the liquid cell, so it is not known what the exact volume of the liquid cell is.

All sample chips are put in an ozone/UV plasma cleaner for at least 20 minutes before liquid cell assembly. One chip is set in the square shaped slot on the liquid cell holder tip with the silicon nitride window facing upward. This chip contains the bottom window. The sample is dropped onto a second chip, again, with its silicon nitride window

facing upward. After chips are cleaned, they are consequently hydrophilic for 2-3 minutes. This allows for a 0.75 μL drop of sample to spread out smoothly over the entire surface of the silicon nitride window of this second chip. It is then flipped and set on top of the first window in the liquid cell holder tip. The tip cover in (Figure 12c) is put over the “chip sandwich” and secured, sealing the two chips together and completing the liquid cell. However, when the chips are sealed, it is likely that some liquid is lost due to the pressure applied to make the seal. This will affect the concentration of the sample.

In preparation for imaging, fluid lines within the holder and fluid lines connecting the liquid cell holder to the reagent syringes are flushed with sufficient amounts of water to remove residual reagents from previous experiments. The smaller fluid lines within the liquid cell holder is consequently filled with water, which is the same matrix used to prepare the nanoprisms. This is of importance since the liquid in the small fluid lines within the holder will be pulled into the liquid cell once the cell is under low enough pressure. This happens twice: once during a vacuum test to check that the liquid cell is sufficiently sealed, and a second time when put into the microscope. This will affect the concentration of the liquid in the cell, but unfortunately this cannot be quantified without complex liquid dynamics simulations. The larger fluid lines are filled with the reagent that will be flowed into the liquid cell. In these experiments, one line was filled with hydroxylamine and the other line was filled with gold precursor (HAuCl_4 solution).

Results and Discussion

Ex situ results

In order to confirm DNA-mediated gold nanoprism morphology experiments could be replicated, TEM images were taken of nanoprisms which were incubated with T30 and then had gold precursor and reductant added *ex situ*. Most of the particles grew to roughly 200 nm, around twice the original diameter of the template nanoprisms (Figure 13a) and >90% have changed into the expected 6-pointed star shape (Figure 13b). The nanostars were around 50 nm thick (Figure 13e), and it was observed that around the edges of the points in both top and side views of the nanostars, there were thinner sections suggesting possible radial growth. Lu et al. imaged intermediates of the particles using SEM. The growth of the particles were stopped at different time points using 1.5 mM mercaptopropionic acid²⁶. If radial measurements were taken during growth it may give some insight on whether or not this radial growth is occurring. In Figure 13c, the thinner sections can clearly be seen on the edges of the points of the stars. Figure 13d shows the thinner sections from the top view. There are two interesting points to note: 1) the growth on the outer points are not consistent around the entire nanostar and 2) the nanostars have stacked on their flat top and bottom {111} faces, which are known to have the lowest free surface energy for nanoprisms. However, it was reported that a drying effect creates false assemblies of these nanoparticles⁵⁸, and it is possible that the stacking is an artifact of the solvent evaporation during the TEM sample preparation. If time had

permitted, one could try to resuspend the nanostars into solvent from the TEM grid and image the sample *in situ*.

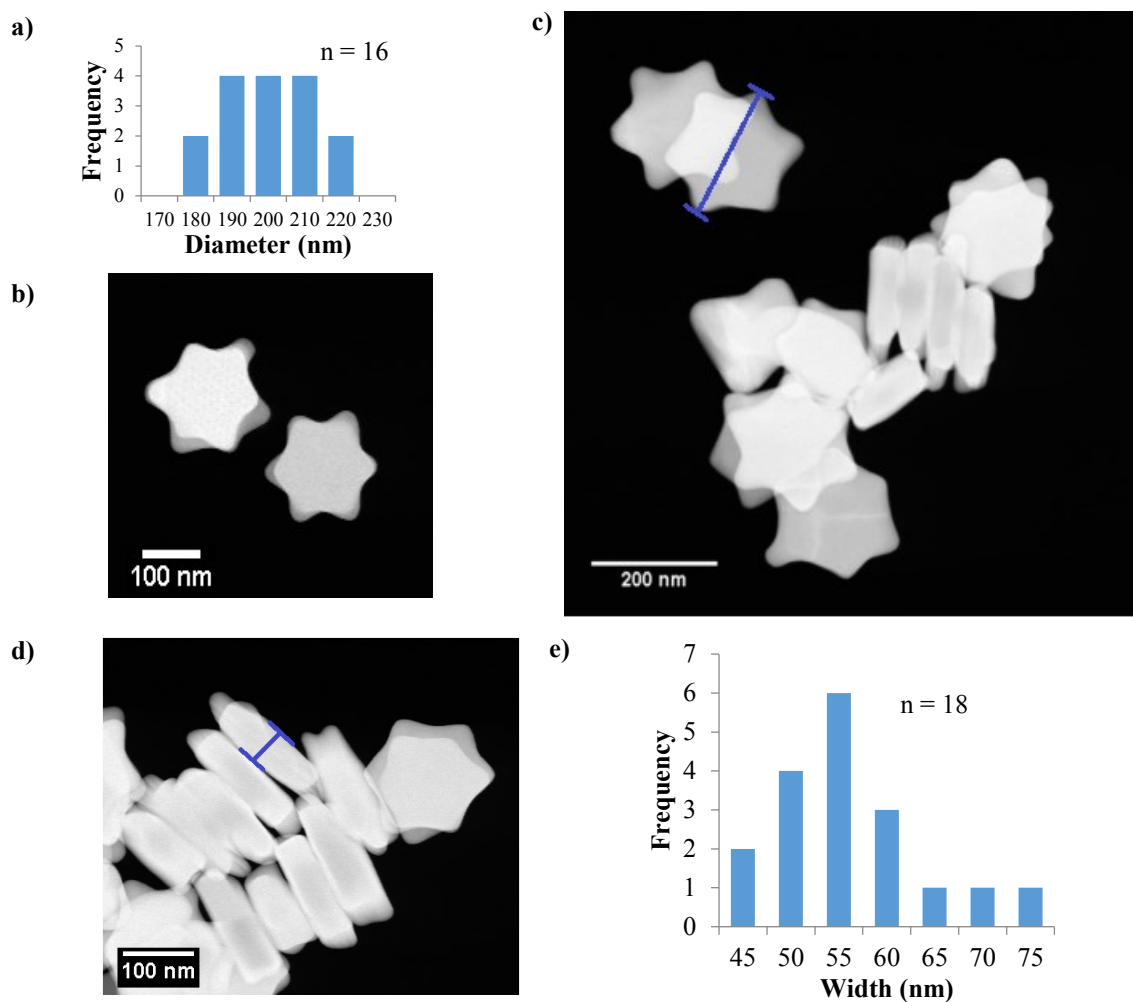


Figure 13 *Ex situ* images of Au-T30 nanostars on a TEM grid **a)** Size distribution by diameter, $n = 16$. Blue measurement bar in (c) shows how diameter measurement was taken. **b)** Single gold nanostars showing thinner sections around the points of the stars **c)** Most nanostars grow to roughly twice the diameter of the gold nanoprism templates. **d)** Some nanostars stacked together on their sides. Again, thinner sections are shown on the peripheral parts of the nanostars. **e)** Width distribution determined from side views of nanostars, $n = 18$. Blue measurement bar in (d) shows how width measurement was taken.

It is not known what parts of the nanoprism templates are preferential for DNA binding. However, it has been reported that thymine has much less affinity for gold surfaces than adenine⁵⁷. Therefore it can be proposed that poly T30 adsorbs onto the

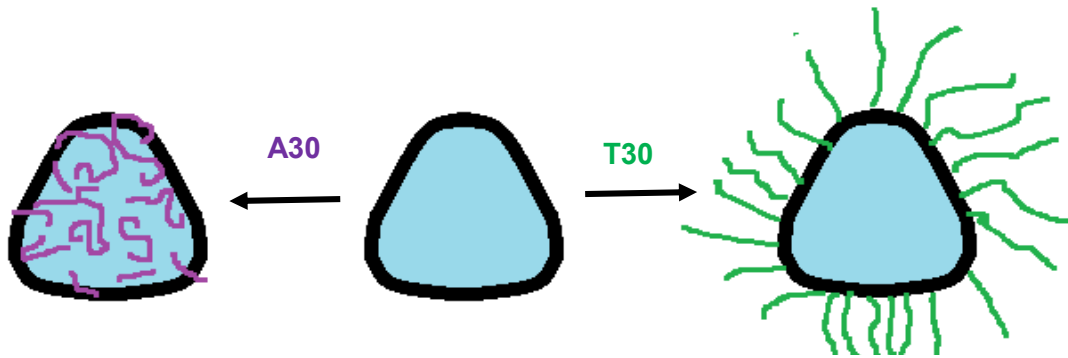


Figure 14 Representation of how T30 might bind to Au NPRism surface compared to A30.

nanoprism surface through the bases much less than A30, if it adsorbs onto those surfaces of the nanoprisms at all. Recall that the synthesis of the nanoprisms uses iodide ion, which prefers to bind to the $\{111\}$ facets of gold that make up the flat faces of the nanoprisms. If during synthesis this had caused CTAB, a cationic surfactant, to form layers more on the sides of the nanoprisms (which are then reduced as much as possible through the etching procedure), it is possible the DNA will preferentially interact on those sides as opposed to the faces, since there is less capping agent present on the sides. If regardless of the type of DNA there are interactions on these sides, then the differences in nanoprism change in morphology should be due to the interactions of the DNA with the broad faces of the Au NPRisms. It was mentioned previously that multiple kinds of gold-DNA interactions and the interplay of those interactions would determine how DNA interacts with the nanoparticles. If the rest of the T30 molecule (other than the part or parts bound to the sides of the nanoprisms) is more coiled than A30, it would follow that due to electrostatic repulsion from the phosphate backbone of DNA the rest of the molecule wouldn't adsorb as well as A30, which would be less coiled and therefore have more exposed bases for more possible probability for successful adsorption interactions.

It would also make sense in this case that the Au-A30 nanoprisms turn into rough disks after growing into the same intermediate hexagonal plates as Au-T30 nanoprisms since A30 surface coverage of the nanoprism would be greater than that of T30. It could be possible that the gold is reduced using the DNA as scaffolding. In the case of A30, the scaffolding would be more on the faces of the nanoprisms compared to T30, creating the rough disk shape.

For comparison, a sample prepared the same way as described in the previous section was imaged using the liquid cell. After Au-DNA nanoprisms were allowed to interact with the gold precursor and reductant *ex situ*, this sample was immediately dropped onto a silicon nitride chip and put into the liquid cell as soon as the DNA incubation period ended. The size of the nanostars are also measured to be around

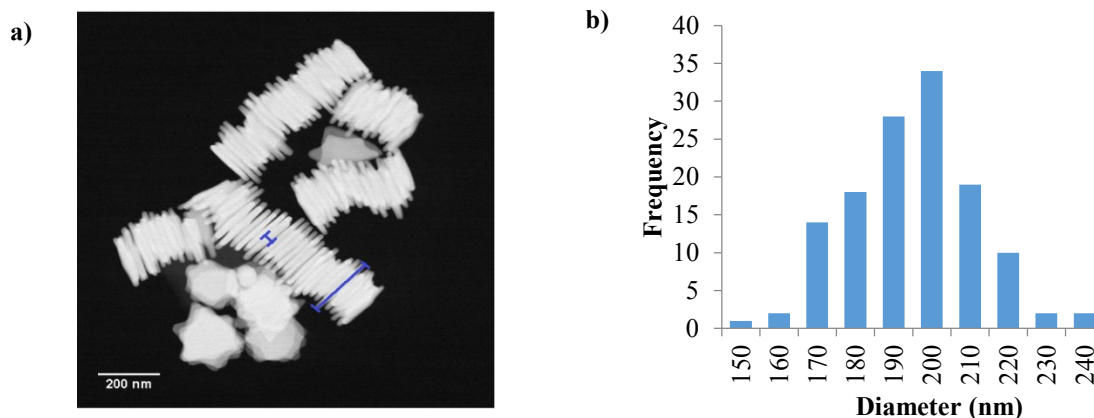


Figure 15 Liquid cell STEM images of *ex situ* synthesized Au-T30 nanostars. **a)** Most of the nanoprisms have turned into the predicted 6-pointed stars. They have stacked, which was also seen on the TEM grid. However, the length of stacks in the liquid cell are much longer. Blue measurement bars show how the width and diameter measurements were taken. **b)** Diameter distribution of T30 nanostars, $n = 130$. Blue measurement bars show how the measurement was taken for both side (Figure 15a) and top (Figure 15c) views.

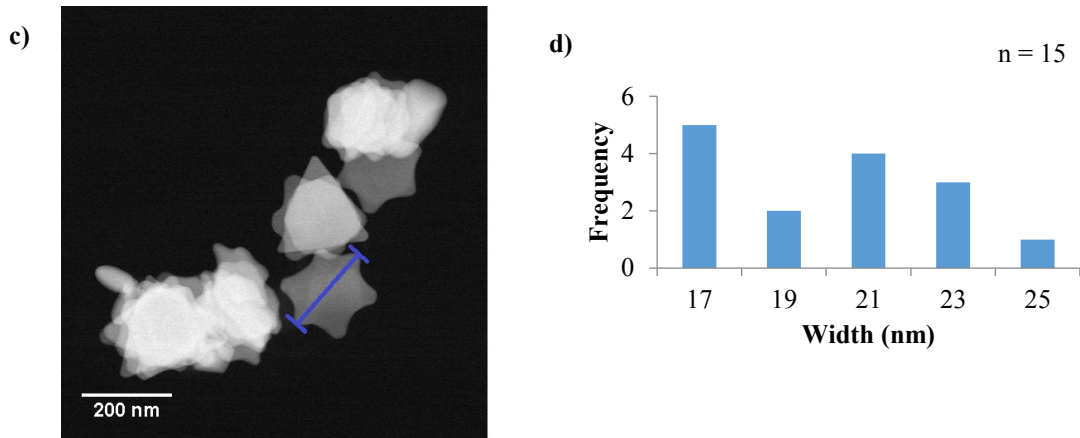


Figure 15 c) A rare few T30 nanostars are seen unstacked. Blue measurement bar shows how the diameter measurement was taken. **d)** Width distribution for T30 nanostars in the liquid cell, $n = 15$.

200 nm, as was the case in the TEM samples (Figure 15b). However, the thickness of the nanostars are markedly smaller at around 20 nm, and the stacks are much longer than on the TEM grid. If drying is causing the nanoparticles to stack as previously mentioned in

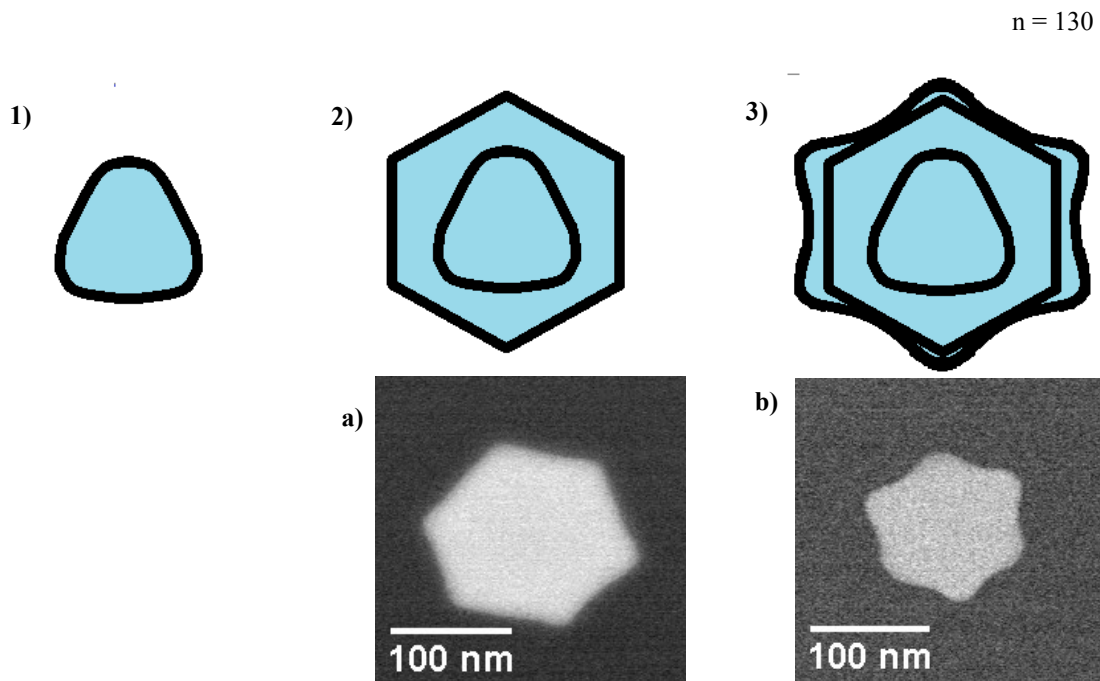


Figure 16 Proposed shape progression for Au-T30 NPrisms. The STEM images below the diagram are from the same sample prepared *ex situ* and immediately put into the liquid cell. The initial nanoprism template is missing, since all nanoprisms showed growth to some extent. **a)** STEM image of a hexagonal plate that did not fully grow into a nanostar. **b)** STEM image of an asymmetrical nanostar, almost completely grown to a full nanostar.

the *ex situ* results, a sufficiently thicker liquid cell could be used to make sure the samples stays wet. Then the sample could be imaged to see if the stacks are still present.

Since a high angle annular dark field (HAADF) detector is used, it can be seen that the nanostars have the bright Z-contrast that is representative of gold nanoparticles and the contrast is mostly consistent throughout the nanostars, indicating relatively consistent thickness throughout most of the nanoprisms. It is seen that there are still some thinner sections on the peripheral parts of the nanoprisms, most easily seen from the side views (Figure 15a). Again, most nanoprisms have changed in predicted 6-pointed star shape (Figure 15a,c). However, a few did not grow completely into 6-pointed nanostars. They grew into hexagonal plates, which agrees with the report that T30 DNA causes the nanoprisms to grow from triangular shapes to hexagonal shapes, and then to the predicted 6-pointed nanostars 26. It is possible the hexagonal shaped particles did not turn completely into 6-pointed nanostars due to dilution of the gold precursor or reductant solution by the water that resided the fluid lines of the liquid cell holder (Figure 16). This could also be the reason for the contrast in width sizes for nanostars dried on a TEM grid compared to those dropped in the liquid cell. The gold (III) ions in solution are still being reduced even after 30 minute reaction period.

Regarding the nanostars in the STEM image for Figure 16, the third step (Figure 16b) shows a little bit of asymmetry that is also seen in the thicker part of the nanostars in Figure 13b. Since the nanoprisms are generally more isosceles triangles instead of equilateral triangle, this asymmetry is feasible, especially when one thinks of how T30 may bind to the nanoprism on the sides instead of the faces.

***In situ* experiments**

After it was confirmed that the nanoprisms could successfully be synthesized and morphed into the desired shaped according to the T30 DNA sequence, *in situ* experiments were attempted to further explore the mechanism of growth. By looking at areas of growth at different points in time during growth, one could find which areas of the nanoprism template are areas that hinder ion reduction or promote ion reduction. Because there are factors that complicate the system within the liquid cell, different parameters had to be tested to achieve nanoprism growth via heterogeneous nucleation. The following experiments used a blank chip with a 250 nm spacer chip for all samples, unless otherwise noted.

Fluid line set up and flow rate

The first set of experiments made use of a y-shaped connector for the reagent fluid lines which allowed simultaneous, continuous flow of 100 μL of 0.2 mM gold precursor in one fluid line and 100 μL of 2 mM hydroxylamine in a second fluid line into the liquid cell at 5 $\mu\text{L}/\text{min}$. Ten minutes after all the reactants were completely flowed in, there was no visual sign of reduction. The particles retained their shape and thickness. After an increase in gold precursor concentration from 0.2 mM to 0.5 mM there was still no evidence of chemical or beam reduction, as evidenced by the lack of homogeneous nucleation in the liquid surrounding the particles. (Figure 17).

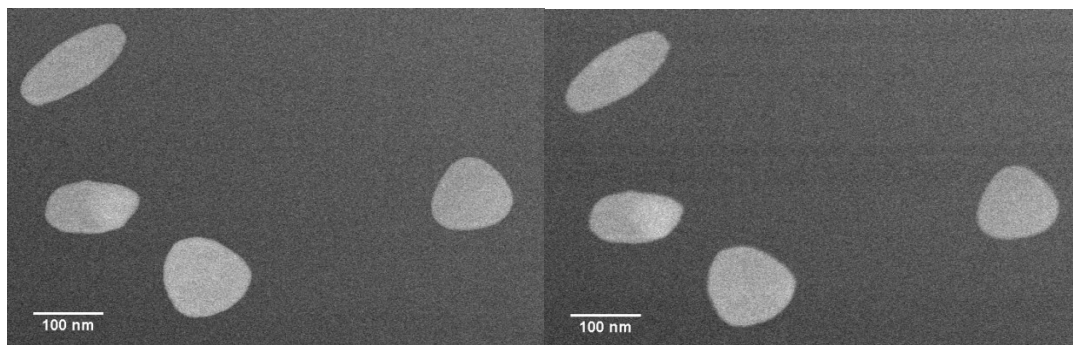


Figure 17 Au-T30 nanoprisms show no change after ten minutes, then another 50 minutes after an increase in HAuCl_4 concentration.

It was hypothesized that reactants were either not reaching the nanoprisms or the gold was being reduced before reaching the nanoprisms in the liquid cell. With the assumption that there was plenty of reductant within the cell at least from the initial sample droplet, flow of reductant was ceased, and only 0.5 mM gold precursor was flowed in after about an hour of no visible change. However, because flow is governed by diffusion, the reductant was likely entering the liquid cell even after the flow rate was stopped. After this increase in gold precursor concentration, both chemical and beam induced change was seen (Figure 18). The rapid growth after no further addition of reagent suggested the gold precursor was delayed in reaching the prisms or was not

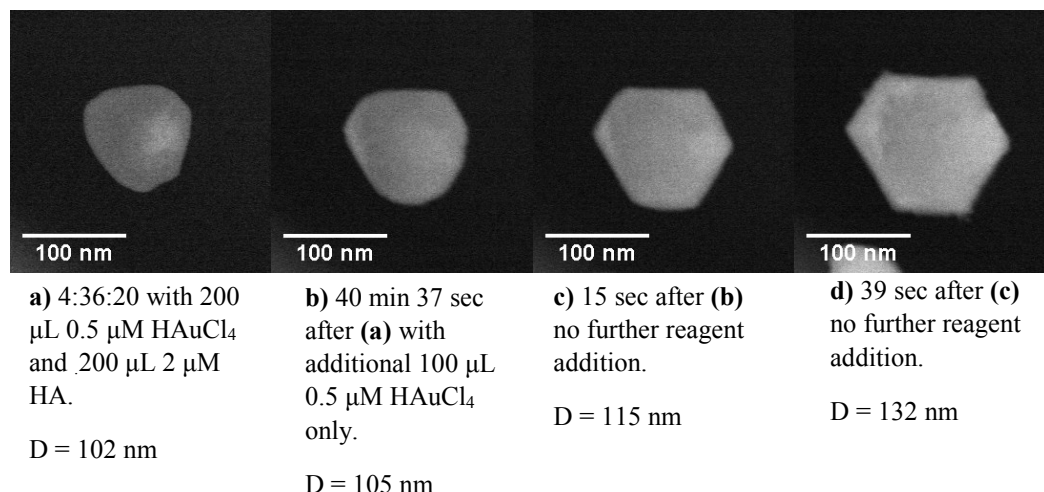


Figure 18 Evolution of Au-T30 NPrism into hexagonal plate. The rapid growth after no further addition of reagent suggests the gold precursor and/or reductant are delayed in reaching the prisms or were not getting a chance to react in the presence of the prisms

getting a chance to react in the presence of the prisms. However, the change from a nanoprism to this hexagonal shape supports the progression shown previously (See “*Ex situ* results”). The increase in gold concentration showed that successful replication of the experiment *in situ* was possible if the gold precursor and reductant could get to the liquid cell.

In order to give the gold precursor less time to be reduced before reaching the nanoprisms, the fluid lines were shortened. The reductant was again set to flow in simultaneously with the gold precursor. There was some evidence that the gold was

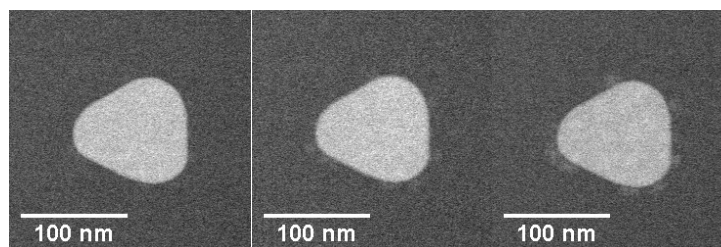


Figure 19 Au-T30 NPrisms: After shortening the fluid lines, it is seen that there are very small particles attaching to the surface of a nanoprism. The gold precursor was being reduced before reaching the nanoprisms. D = 103 nm for all images of the same particle. Second image taken 27 seconds after the first. Third image taken 6 seconds after the second image.

indeed being reduced before reaching the particles. Contrast indicating very small particles on the surface of the nanoprism could be seen that got brighter with more time and beam exposure (Figure 19).

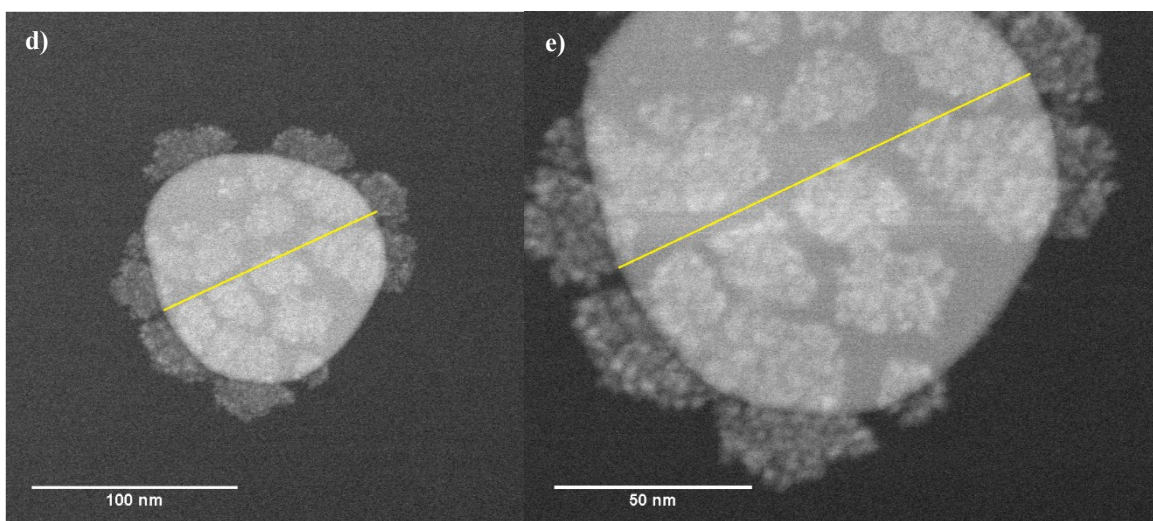
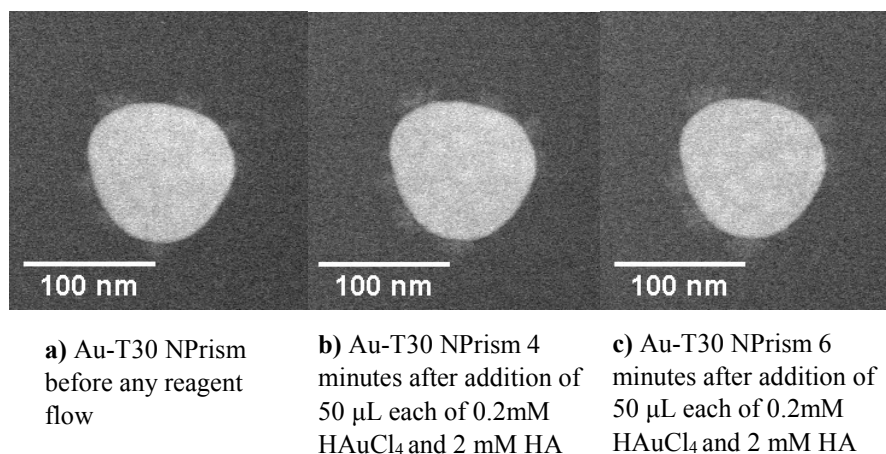


Figure 20 (a-c) The nanoprism retains its shape while small nucleated particles accumulate on the surface. $D = 106$ nm for all images of the same particle. These images taken within 30-40 seconds of each other. **(d-e)** Higher magnification reveals that the fuzziness shown on the surface is made of clusters of approximately 2-5 nm homogeneously nucleated particles that have attached to the nanoprism. Images taken 27 seconds apart. $D = 114$ nm in all images for the same particle. Yellow line shows how the measurement was taken.

Higher magnification showed the particle layer was composed of \sim 2-5 nm gold nanoparticles, suggesting that the gold precursor and hydroxylamine may have been homogeneously nucleating in the fluid lines and then attaching to the nanoprism surface

(Figure 20). However, it is possible that these clusters of small particles are pre-nucleation clusters that will form a new surface of the nanoprism.

Since the gold precursor concentration was obviously high enough to create homogeneous nucleation, it is possible enough reductant and gold precursor were in the liquid cell and the nanoprisms were not preferred as surface sites for heterogeneous nucleation. However, if more gold precursor had been added to the liquid cell, nanostars formation could still be a possibility if the nucleation is not described by the classical nucleation pathway. These small particles could be pre-nucleation clusters that will later form the new nanoprism surface. There was no change in size for any of the nanoprisms, regardless of the amount of 2-5 nm particles attached to their surfaces. It is difficult to conclude whether these clusters were arrived at the nanoprism surface. The next factor to consider was the flow rate of the reagents.

The flow rate of reagents provides a constant renewal of the solution in the liquid cell environment. All the previously mentioned experiments were run with a reagent flow rate of 5 $\mu\text{L}/\text{min}$. With the assumption that the gold precursor was being reduced too quickly, maybe because of the electron beam, the flow rate was increased from 5 $\mu\text{L}/\text{min}$ to 10 $\mu\text{L}/\text{min}$. However, it is now known that actually decreasing the flow rate will produce the desired effect of delivering reagents to the liquid cell, since the process is limited by diffusion. Some of the smaller particles that had already attached to the nanoprisms were washed away, as well as any free homogeneously nucleated particles in the surrounding liquid. There was still no change in nanoprism morphology. Further work should be done at much slower flow rates to allow diffusion to deliver the reagents.

Alternating reagent addition

To get a more controlled sense of what comprised the liquid environment in the liquid cell, the y-shaped connector was removed and gold precursor and reductant were alternately flowed into the liquid cell in separate fluid lines. 100 μL of reductant was added to wash as many homogeneously nucleated particles as possible and subsequently 100 μL of gold precursor was added. Flow rates for both reagents was 10 $\mu\text{L}/\text{min}$. Very slow growth was observed (Figure 21 a-e).

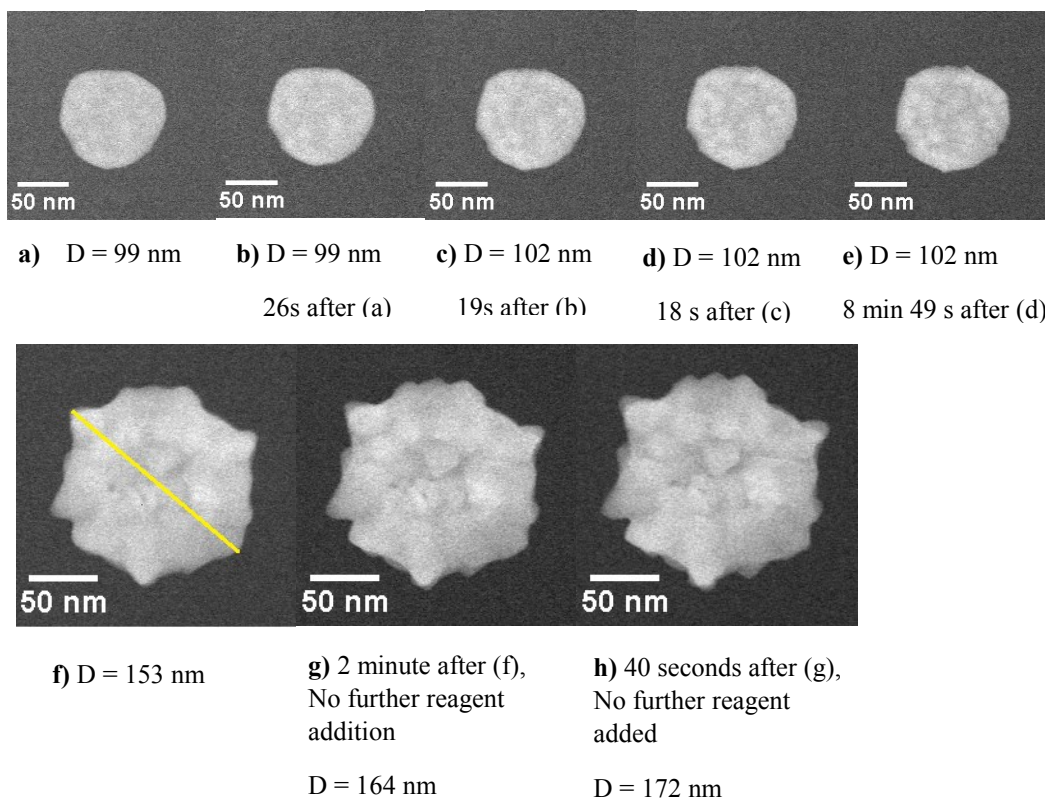


Figure 21 Au-T30 NPrisms: Removal of the y-connector to flow reagents in alternately and at a higher flow rate initiated slow growth after washing away most of the homogeneously nucleated particles. **a)** After the addition of 100 μL each of 0.2mM HAuCl_4 and 2 mM HA. **b)** After addition 75 μL of 0.2 mM HAuCl_4 to ensure reaction of all reductant in the liquid cell. **c-d)** No further reagent addition. Au-T30 NPrisms at higher flow rate and alternate reagent addition. **(f)** taken 13 minutes after **(e)** was taken with no further reagent addition.

To ensure all the reductant was reacted or pushed out of the fluid cell, another 75 μL of gold precursor was added, and there was much more significant morphology change (Figure 21 f-h). It was concluded that reagents should be flowed in alternately rather than simultaneously to better control the composition of the liquid cell environment and also to ensure reaction in the liquid cell and not within the lines. Since flow is diffusion limited, a y-connector should not be used to have both reagents flowed into one fluid line. It cannot be known how equally the two reagents are distributed within the lines without more extensive modeling experiments.

Effect of liquid cell volume on flow and liquid cell environment

With all the difficulties in getting reagents to the liquid cell, an experiment was done to see whether a larger liquid cell would give insight on how the reagents travel within the fluid lines to the liquid cell holder tip. Some predicted outcomes were: 1) homogeneously nucleated particles would rapidly grow and accumulate due to the larger liquid layer, providing many electrons for reduction, 2) nanoprisms would successfully change into desired morphologies which would just be imaged at lower spatial resolution, or 3) the reagents flow very well through the liquid cell, but push out the reagent that was flowed in previously, causing no reduction of ions in the liquid cell. Lower concentrations of hydroxylamine (0.5mM) and gold precursor (0.2mM) were used in an attempt to prevent rapid homogeneous nucleation.

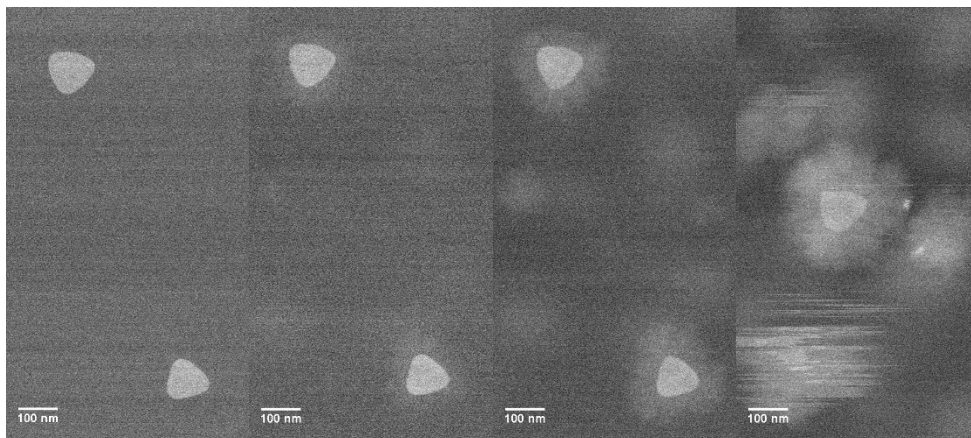


Figure 22 Nucleated particles can be seen forming fuzzy contrast on the nanoprism surfaces as well as in the surrounding liquid environment.

It was found that with plenty of flow through a large liquid cell comprised of a 500 nm spacer, 600 nm polystyrene beads, and a blank chip (1.1 microns total) the nucleation of the 2-5nm particles still occurred (Figure 22). Without a video in real time, it is difficult to see whether they are homogeneously nucleating and attaching or pre-nucleating on the surface of the nanoprism. Additionally, nanoprisms started to detach from the silicon nitride windows due to the liquid flow (5 $\mu\text{L}/\text{min}$). Additionally, as predicted, the spatial resolution is much worse than with thinner liquid cells.

Conclusion

A series of preliminary experiments were carried out in order to attempt to visualize the growth of T30 DNA-mediated nanostars from nanoprism templates. An attempt to simulate the reaction environment of an *ex situ* experiment in which triangular gold nanoprisms changed shape into 6-pointed stars was made, although the environmental factors within a liquid cell are very different from those in an *ex situ* experiment. These factors are difficult to quantify without extensive work and complex

simulations. The dynamics of fluid flow within the liquid cell should be studied as well as a closer look into how different types of DNA may bind to the nanoprism template. This was achieved via the use of a liquid cell holder that encapsulates a “chip sandwich” acting as the liquid cell. This closed system allows the sample to be put under the vacuum environment, but still allow the transmission of electrons required for STEM imaging.

First, the replication of *ex situ* growth of Au-T30 nanoprisms was confirmed by TEM imaging. The expected rounded triangle shapes of the nanoprism templates grew into the expected 6-pointed nanostars around 200 nm in diameter and 50 nm in width. The TEM image showed thinner sections on the ends of the points suggesting radial growth. These results were also seen using STEM and the liquid cell, although the widths of the nanostars were less than half the widths of the nanostars imaged using TEM. It is hypothesized that the growth is abbreviated in the liquid cell because the reagents may get diluted due to the extra liquid that is taken in from the fluid lines of the liquid cell holder.

Next, the experiments were attempted to be replicated *in situ* in the liquid cell using STEM imaging. The transition from *ex situ* to *in situ* experiments is challenging, since many factors contribute to the chemical environment within the liquid cell. This is due to the fact that in the liquid phase there are factors that can hinder the efficiency of chemical reduction of the gold precursor: (1) the electron beam and radiolysis products of surrounding water provide significant sources of reduction for gold (III) ions in solution could lead to preferential homogeneous nucleation instead of heterogeneous nucleation using the nanoprisms as the sites of growth, 2) the liquid cell creates a dynamic and less controllable environment for the gold precursor and the reductant since they have to be

added by way of microfluidic lines, and 3) the concentrations of gold precursor and reductant can be diluted due to the water contained within the fluid lines of the liquid cell holder, impeding efficient growth.

A series of experiments were performed in an attempt to overcome these factors and promote a liquid environment conducive to heterogeneous nucleation rather than homogeneous nucleation. Parameters explored were: 1) fluid line set up and flow rate, 2) simultaneous and alternating reagent addition, and 3) effect of liquid cell size on reagent flow and liquid environment.

Future work should focus on optimizing other parameters that allow a liquid phase environment conducive to preferential heterogeneous nucleation. For example, if a liquid cell holder allowed the simultaneous flow of reagents into two different fluid lines, the potential for reagents to react within the fluid lines would be eliminated. Additionally, the gold precursor and reductant would be near the preferred site of nucleation, promoting heterogeneous nucleation. The concentrations of gold precursor and reductant should be present in the liquid cell in quantities sufficient enough to initiate growth, but not so high that homogeneous nucleation dominates the system.

CHAPTER 3

COMPARING THE BINDING OF T30 AND A30 DNA TO GOLD NANOPARTICLES

Introduction

As mentioned previously, the nature of how DNA interacts with the gold nanoparticle surface affects the growth mechanism into a new shape. The DNA used in this work is non-thiolated, single-stranded DNA. Since this DNA is not in a stable double helix like double-stranded DNA, the DNA bases are not kept shielded on the inside of the molecule. This exposes the bases and enables them to be able to interact chemically, electrostatically, and through the hydrophobic effect. Additionally, the absence of the thiol group takes away its proven ability to covalently bind to gold nanoparticle surfaces. This study compares the binding affinity of each oligonucleotide to ~13 nm gold nanospheres. Previous studies on the single bases suggest thymine bases will have weaker binding affinity to gold nanoparticles compared to adenine bases^{34, 57, 35}.

The binding of uncharged molecules to gold nanoparticles has been reported to produce an LSPR peak red-shift when the nanoparticles agglomerate⁵⁷. In 2002, Storhoff et al. monitored the LSPR peaks of ~16 nm gold nanoparticles that had been incubated with thiolated deoxynucleosides (dA, dG, dC, and dT)⁵⁷. After an hour of incubation with the gold nanoparticles, the LSPR band of dA red-shifted while the LSPR for dT did not change. It was assumed that the lack of agglomeration related to the lack of binding from the dT (Figure 23). Similar results were reported using polynucleotides of 5, 10, 15, and 20 adenine, thymine, and cytosine bases⁵⁷.

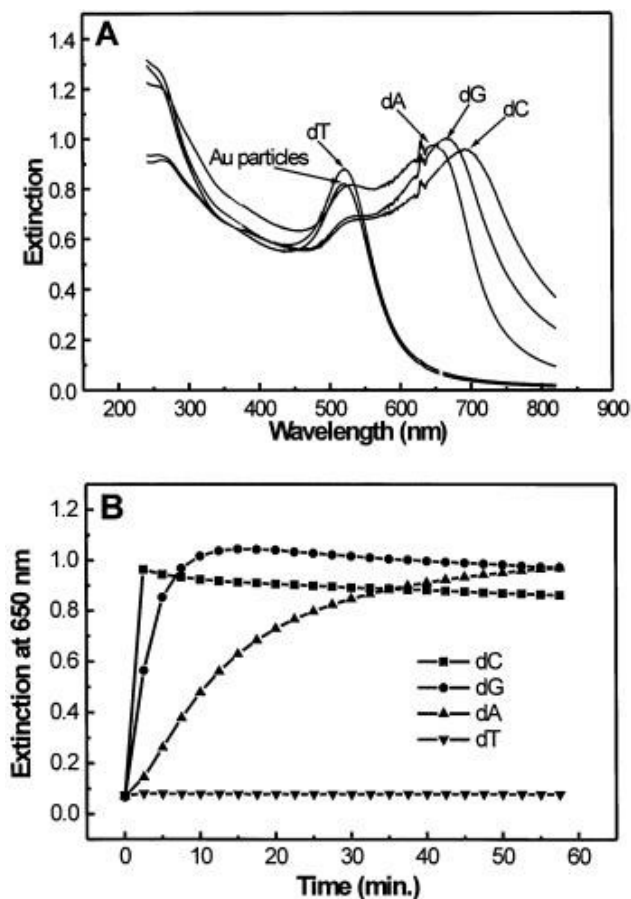


Figure 23 (A) Absorption spectra of separate Au nanoparticle solutions containing one of the deoxynucleosides (dA, dC, dG, or dT). (B) Kinetics of nanoparticle agglomeration of Au nanoparticle solutions containing dA, dC, dG, or dT followed by monitoring the extinction changes at 650 nm as a function of time 57. Reprinted with permission from [57] Storhoff, J. J.; Elghanian, R.; Mirkin, C. A.; Letsinger, R. E. *Langmuir* **2002**, *18*, 6666-6670. Copyright 2002, American Chemical Society.

Nelson and Rothberg reported through fluorescence studies that polynucleotides of 15 thymine bases did not bind as much as polynucleotides of 15 adenine bases³². This was shown through the assumption that binding of the dye-modified oligonucleotides would cause quenching of the fluorescent signal. The fluorescence signal for the A15 was quenched to a lesser degree than the T15.

Additionally, Kimura-Suda et al. collected FTIR spectra of A25, T25, and combinations of A5+T25 and A25+T25 and compared them to collected spectra of T25 and A25 only⁵⁹. Comparisons of the spectra suggested that adenine polynucleotides

(A25) had a higher binding affinity than thymine polynucleotides (T25) to gold polycrystalline films in competitive base-specific adsorption experiments. A subsequent report from the same group showed more FTIR and XPS spectra using “blocks” of varying combinations of adenine and thymine polynucleotides, which further suggest that adenine polynucleotides adsorb to more of the gold films than thymine polynucleotides since the surface density is shown to be higher for the poly-adenine⁶⁰.

In the same year, Demers et al. used temperature programmed desorption (TPD) and reflection absorption Fourier transform infrared spectroscopy (RAIR) to obtain heats of desorption of DNA bases and nucleosides on gold films³⁴. Results show desorption energies of 111 ± 2 kJ/mol (TPD) and 110 ± 2 kJ/mol (RAIR) for thymine and 131 ± 3 kJ/mol (TPD) and 129 ± 4 kJ/mol (RAIR) for adenine. They also show desorption energies of 109 ± 3 kJ/mol for thymidine (RAIR, thymine nucleoside) and 112 ± 4 kJ/mol for adenosine (RAIR, adenine nucleoside).

Both T30 and A30 ssDNA interactions with ~ 13 nM gold nanoparticles were characterized using zeta potential, absorption spectroscopy, and isothermal titration calorimetry (ITC). Stability of the nanoparticles after incubation with T30 or A30 indicates binding of the DNA to the nanoparticle surfaces. The zeta potential should indicate if T30 or A30 stabilizes gold nanoparticles. A stable nanoparticle should have a zeta potential $> \pm 30$ mV. Flocculation tests should show minimal shifting of the gold LSPR peak if T30 or A30 stabilizes the gold nanoparticles. Finally, a measure of the binding enthalpy gives a quantity to the degree of binding of T30 and A30 to gold nanoparticles.

Experimental Procedures

~9 nM citrate-capped gold nanoparticle synthesis

A method based on synthesis by Grabar et al. was used to synthesize ~13 nM gold nanoparticles⁶¹. All glassware was washed using aqua regia composed of 3 parts hydrochloric acid and 1 part nitric acid (CAUTION: Aqua regia is a powerful oxidizing agent and it should be handled with extreme care!). In brief, 500 mL of 1mM HAuCl₄ was brought to a rolling boil and 50 mL of 38.8 nM trisodium citrate was added quickly, changing the color from a pale yellow to a wine red. Boiling was maintained for another 10 minutes with stirring. The colloid solution was then cooled to room temperature.

Zeta potential measurements

The zeta potential of a nanoparticle is a measure of the surface charge of the nanoparticle. A Malvern Nano HT Zetasizer with a 532 nm laser was used for all measurements. The gold colloid solution was brought to a pH of 7.6-7.8 using 1M NaOH and measured without dilution. 150 μ L each of 100 μ M T30 and 100 μ M A30 in 1X Tris-EDTA buffer, pH 8.0 were incubated with 3 mL of ~13 nM gold nanoparticles for 1 hour. All measurements included at least 13 runs. Each sample was measured five times.

Flocculation tests using absorption spectroscopy

An Agilent 8453 UV-Visible Spectrophotometer was used to take the absorption spectra of all samples from 190 nm-1100nm. A quartz cuvette was used with a pathlength

of 1 cm. 1 mL samples of a 1-to-4 dilution of as-prepared nanoparticles were incubated with 10-50 μL of T30 and A30 DNA for 4 hours at room temperature, and the absorbance spectra were collected (“Results and Discussion, Figures 24 and 26). 10 minutes after the addition of 500 μL 2M NaCl, the absorbance spectra were collected again (Results and Discussion, Figures 25 and 27). Absorption spectra of gold nanoparticles without the addition of DNA were collected as a control experiment.

Isothermal titration calorimetry (ITC)

A Malvern MicroCal VP-ITC Isothermal Titration Calorimeter (Northampton, MA) was used for these experiments. For each experiment, 48 injections of 6 μL of either 600 nM T30 or 260 nM A30 DNA were added to ~ 1.4 mL of ~ 9 nM gold nanoparticles of $\text{pH} \approx 8$. Initially, 600 nM A30 was also used, but the heat quantities released from each injection were too large to obtain evidence of what kind of binding curve was present. The heat flow vs. time curve could be interpreted to show either immediate saturation of the nanoparticles or a very small degree of binding. Therefore, the concentration of A30 was decreased to confirm that there was in fact little to no binding. The experiments were performed at 25°C using a reference power of 18 $\mu\text{Cal}/\text{sec}$ and a stirring rate of 310 rpm. The binding curve data for AuNPs with A30 were fitted using *ORIGIN* data analysis software (MicroCal, Northampton, MA).

Results and Discussion

Zeta potential measurements

Sample	Z-potential (mV)	Standard Deviation (mV)
~13 nM Au nanoparticle	-26.22	3.59
~13 nM Au nanoparticle with T30	-25.74	2.13
~13 nM Au nanoparticle with A30	-22.15	3.02

Table 1 Zeta potential values for ~9 nM gold nanoparticles with and without T30 and A30 DNA

Stable nanoparticles are expected to have a magnitude $> \pm 30$ mV if they are very stable. Additionally, the addition of DNA is expected to stabilize the gold nanoparticles. These data do not support these observations. Rather, these data suggest that T30 and A30 do not interact or very weakly interact with the gold nanoparticle surfaces.

Flocculation tests using absorption spectroscopy

Addition of DNA to gold nanoparticles is reported to stabilize the particles, so there should also be a resistance to agglomeration upon the addition of salt, suggesting stabilization of the nanoparticles. It can be seen that the LSPR peak for gold at ~520 nm and the absorption peak for DNA at ~260 nm are present before the addition of 2M NaCl for both T30 and A30 (Figures 25 and 27). After the addition of 2M NaCl to A30, there is a gold LSPR peak red shift to ~680 nm for the lower concentrations of DNA while the gold LSPR peak shift for higher concentrations of DNA is only to ~620 nm (Figure 25).

This is in contrast to the peak shifts that are seen when 2M NaCl is added to the gold nanoparticles with T30 DNA, where all concentrations of T30 caused the LSPR peaks of gold to shift to ~ 675 nm (Figure 27). This suggests that at higher

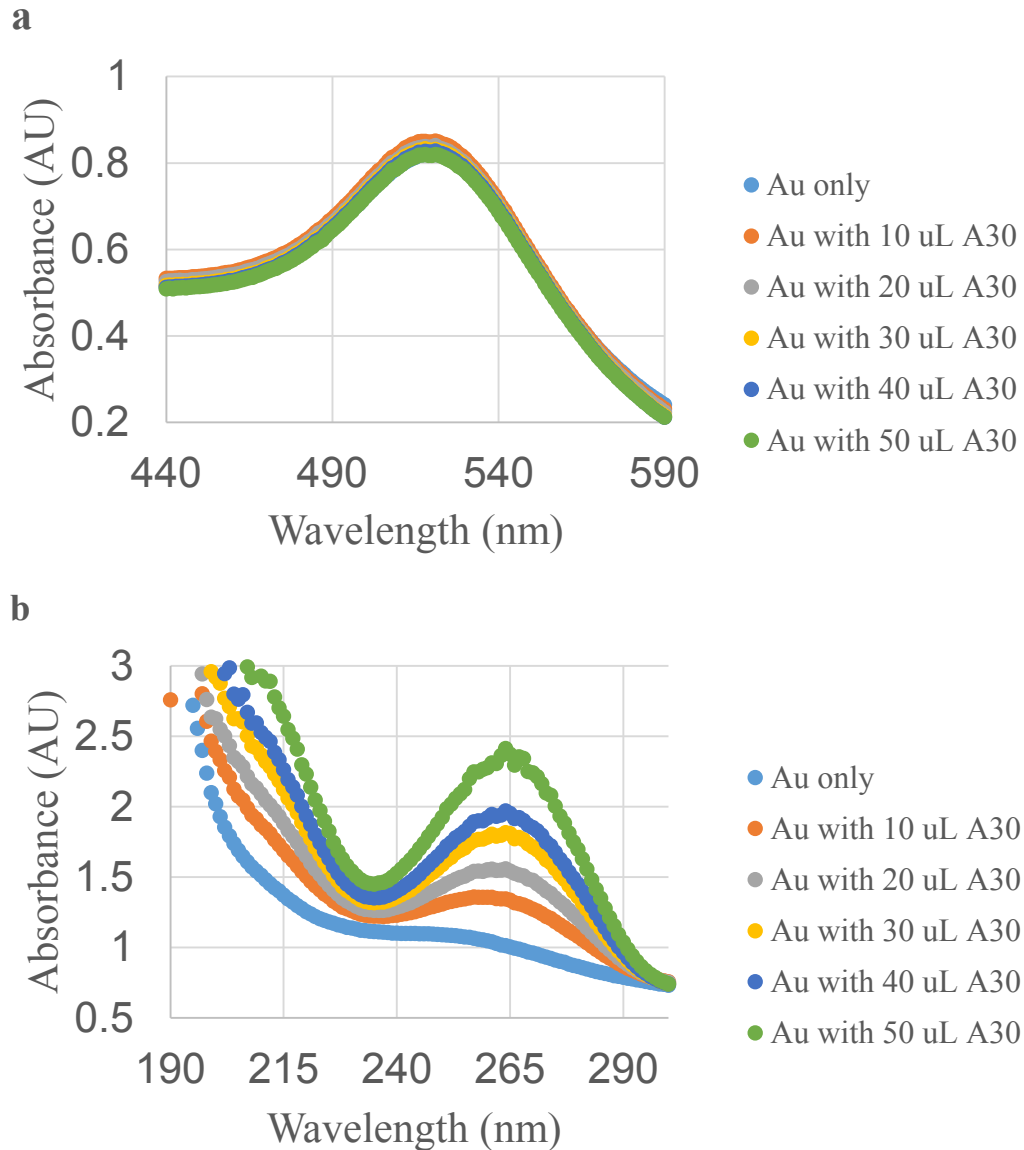


Figure 24 Absorption spectra of ~ 9 nM gold nanoparticles with A30 DNA before addition of 2M NaCl. (a) Localized surface plasmon resonance peaks for the gold nanoparticles (~ 520 nm). (b) Absorption peak for DNA (~ 260 nm).

concentrations, there may be more stability given to AuNPs incubated with A30. At lower concentrations of A30, there is less stability and the agglomeration behavior is similar to that of T30.

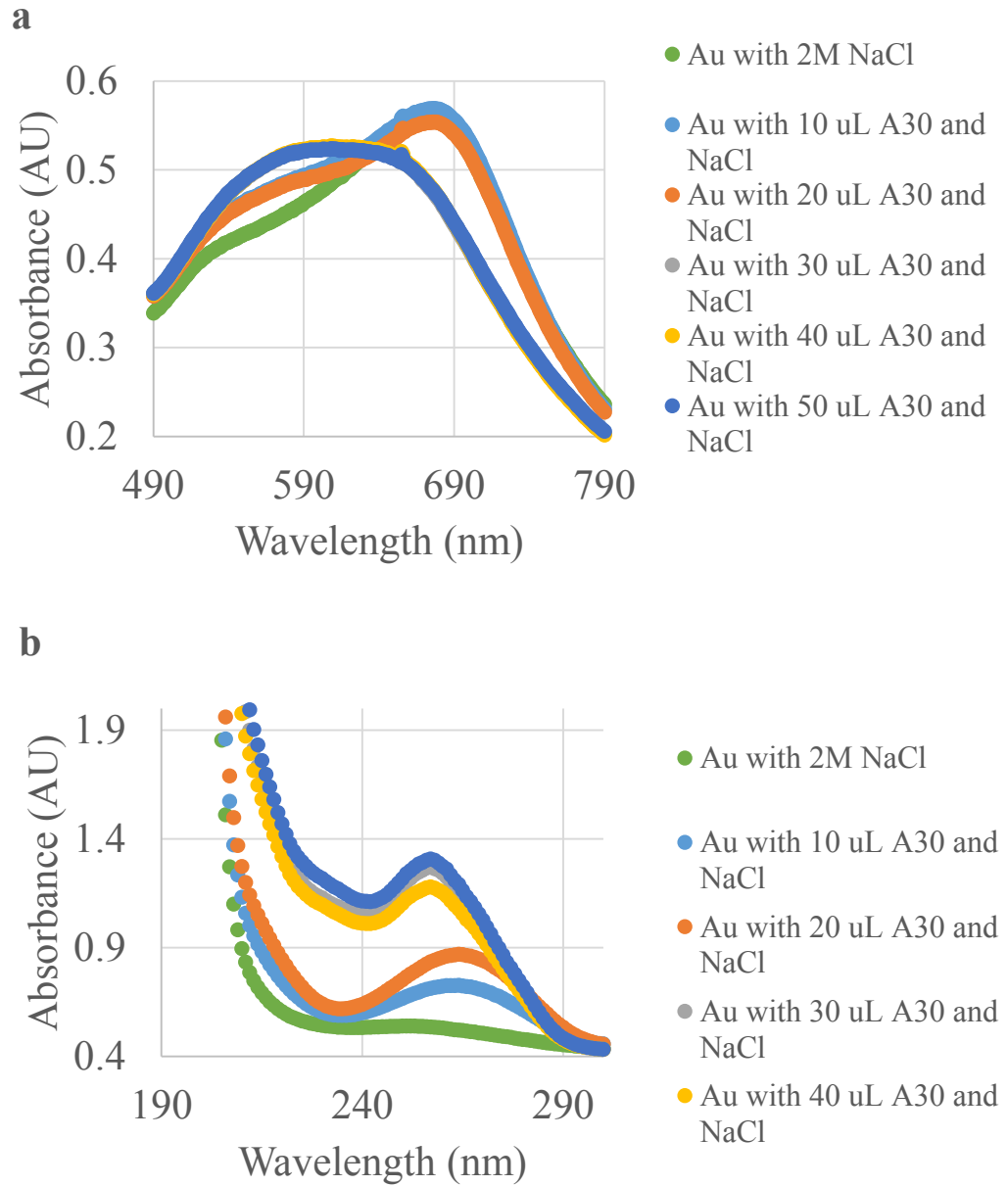


Figure 25 Absorption spectra of ~9 nM gold nanoparticles with A30 DNA with addition of 2M NaCl. (a) Localized surface plasmon resonance peaks for the gold nanoparticle. (b) Absorbance peaks for DNA (~260nm).

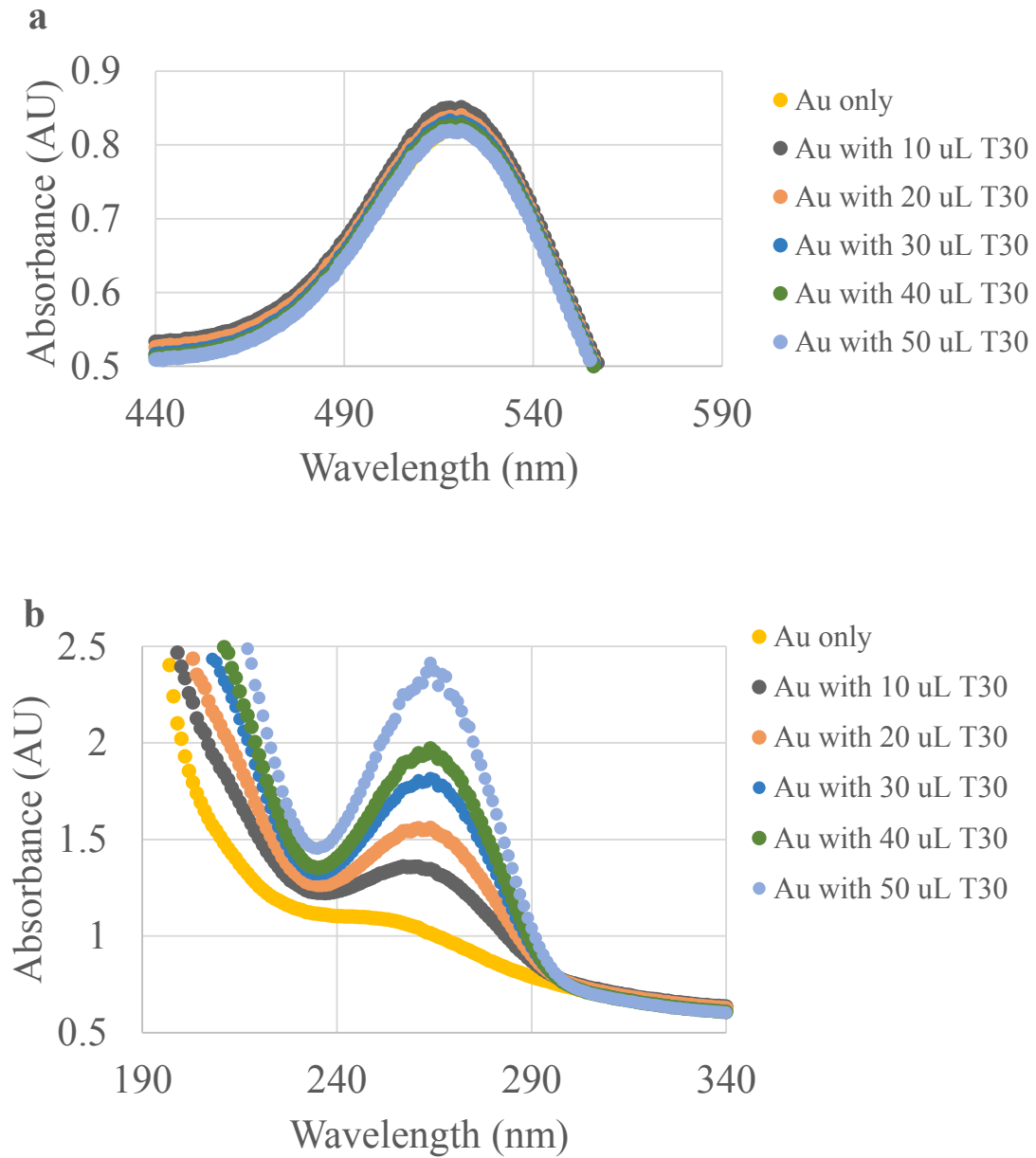


Figure 26 Absorption spectra of ~ 9 nM gold nanoparticles with T30 DNA before addition of 2M NaCl. (a) Localized surface plasmon resonance peaks for the gold nanoparticles (~ 520 nm) (b) Absorbance peaks for the gold nanoparticles (~ 260 nm)

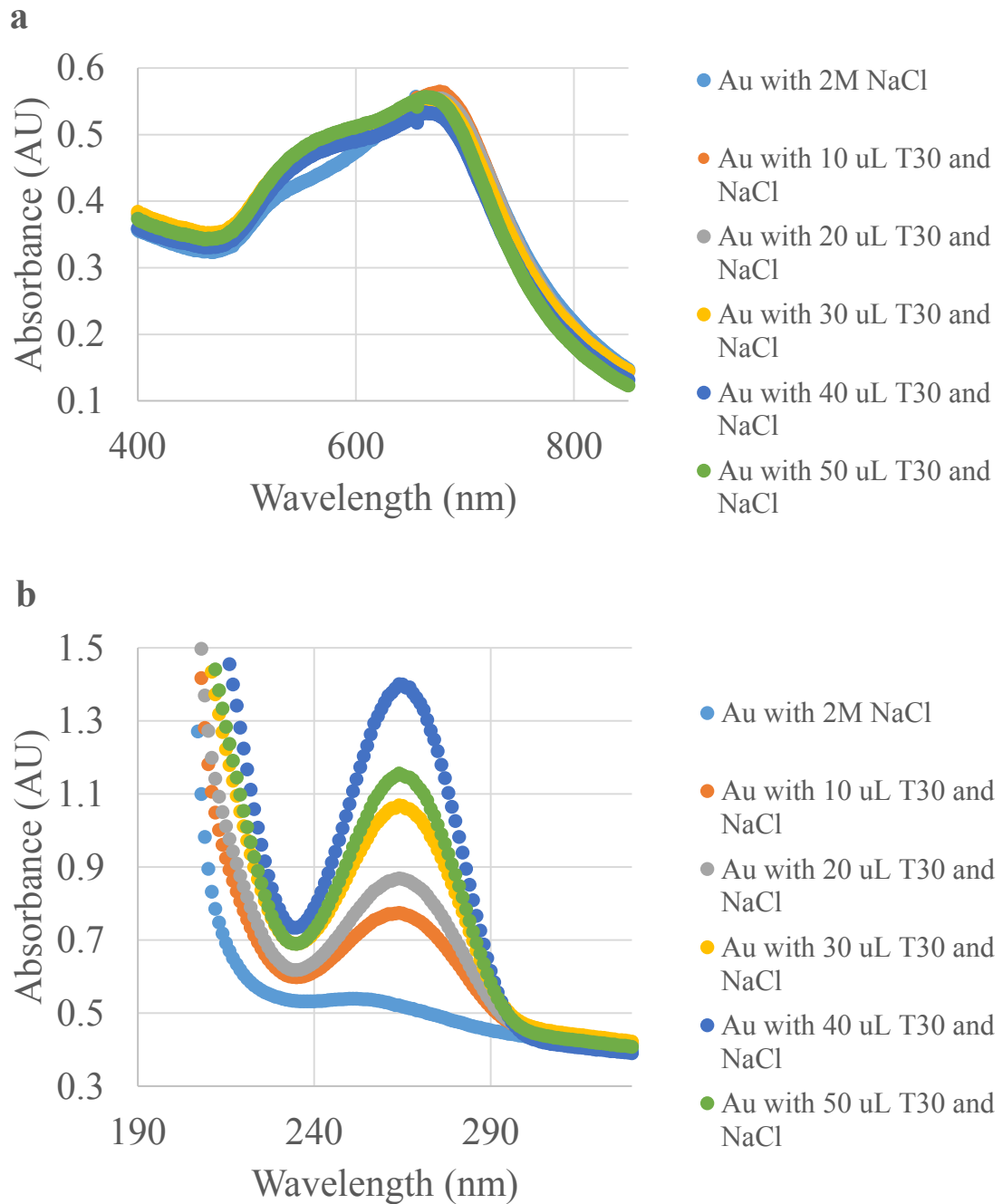


Figure 27 Absorption spectra of ~ 9 nM gold nanoparticles with T30 DNA after addition of 2M NaCl. (a) Localized surface plasmon resonance peaks for the gold nanoparticles (b) Absorbance peaks for DNA (~ 260 nm).

Isothermal titration calorimetry (ITC) experiment to obtain binding enthalpy data

In order to quantify the binding affinity of T30 with gold nanoparticles and compare it to that of A30, isothermal calorimetry (ITC) experiments were carried out. ITC measures the heat of reaction by allowing one to measure the heat quantities absorbed or released upon injections of finite volumes of a ligand to a host species. In this case, the host is the gold nanoparticle solution, which was used without dilution (~9 nM). The ITC consists of two identical cells: one is a reference cell and the other is the sample cell. They are enclosed in an adiabatic jacket and they are very highly efficient thermal conductors. The ITC will detect the difference in temperature between the cells when heat is absorbed or released from the interactions between host and ligand. When enough injections have been added to the host to saturate the host with ligand, the heat quantity per injection should be constant. In this case, when T30 or A30 have no more surface area with which to bind on the gold nanoparticles, the host is saturated. This is seen where the peaks form a plateau in the plots with heat flow vs. time. The data can then be analyzed and fit to different binding curves for different numbers of binding sites,

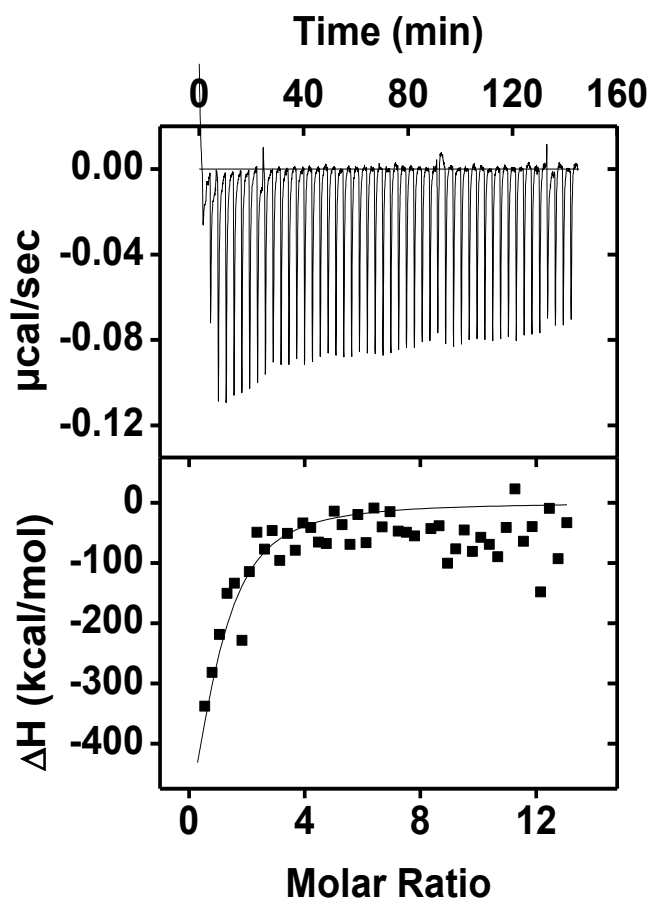


Figure 28 Calorimetric titration of 600 nM T30 into ~9 nM gold nanoparticles. (top) Heat flow as a function of time. (bottom) Binding curve showing heat change per mole of T30. The line of fit represents one site of binding. Heat from water to gold nanoparticles and 600 nM T30 to water has been subtracted to ensure the enthalpy is solely from the DNA to gold interaction.

competitive binding, and dissociation. For the experiments discussed here, only the binding constant and enthalpy of binding are sought after.

In the case of T30 DNA, it was expected from the absorption data and also from the literature that there would be no binding or very weak binding. However, there is a well fit binding curve for multiple concentration runs. The binding constant K_A is 1.23×10^8 M and the binding enthalpy value is $\Delta H = -9.19 \times 10^5$ kcal/mol. On the other hand,

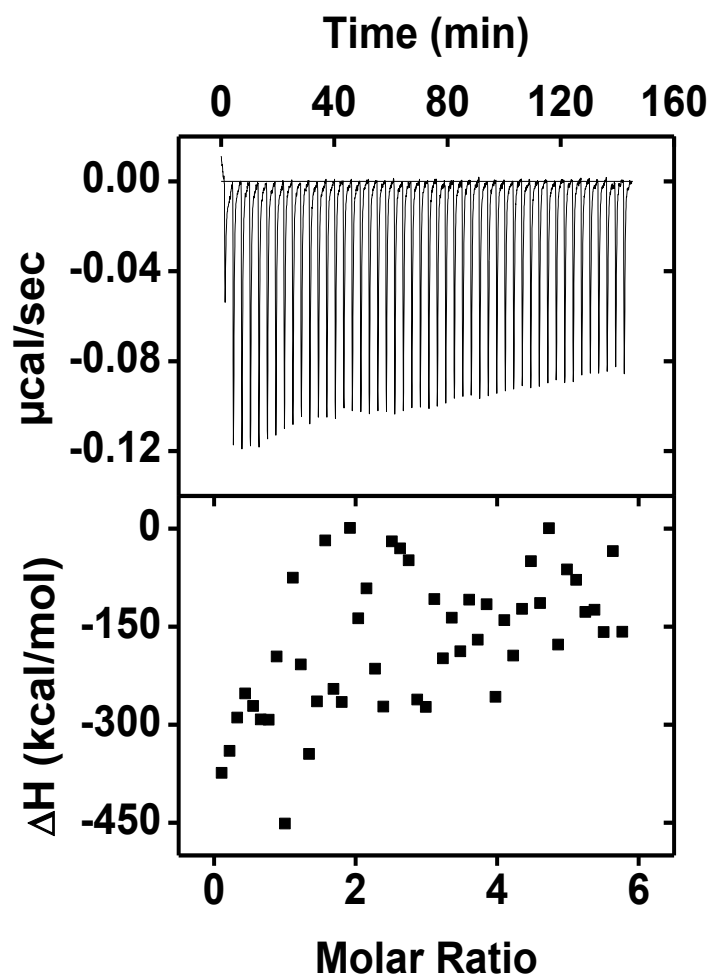


Figure 29 Calorimetric titration of 260 nM A30 into ~9 nM gold nanoparticles. (top) Heat flow as a function of time (bottom) Binding curve showing heat change per mole of A30. Heat from water to gold nanoparticles and 260 nM A30 to water has been subtracted to ensure the enthalpy is solely from the DNA to gold interaction.

A30 DNA, which was expected to have some binding activity showed no binding over multiple concentration runs.

Although the ITC data presented herein suggest T30 has more binding affinity than the A30 DNA, it is suggested that there is some evidence to the contrary in the literature, as discussed previously in the introduction of this chapter.

There are some significant sources of error to consider. First, as evidenced by the zeta potential data, the gold nanoparticles used in this study were not very stable and suggested that neither T30 nor A30 were changing the surface charge of the nanoparticles. Secondly, ITC is very sensitive to differences in pH between the ligand and the host solutions, because there can be some appreciable heat that is detected simply from a difference in pH. It is difficult to measure the exact pH of the gold nanoparticles and keep it constant throughout the ITC experiments, which would ideally have had a buffered matrix. This is not feasible in the case of as-prepared gold nanoparticles of this size, since addition of salt causes immediate agglomeration. Additionally, typical ITC experiments use concentrations on the micromolar scale. Although a binding curve with a decent fit was acquired, the concentrations of ligand and the host were pushing the limits of this particular instrument.

Conclusion and Future Directions

The results from this study are not conclusive, although more useful data could be acquired using ITC, especially if the problem of gold colloid stability in pH values suitable for the binding of oligonucleotides could be solved. A significant obstacle is not being able to use a buffer to create a more stable system while the binding curve is acquired. Finally, the chosen type of gold nanoparticles used for the ITC experiments presented herein were ~13nm gold nanospheres. They serve to represent a simple host that is easily and reliably synthesized, but the simplicity of the morphology may be hindering more easily detectable interactions that would be present in anisotropic nanoparticles. However, the data presented here provide a good starting point for general comparisons of A30 and T30 binding affinities to gold nanoparticle surfaces. Recall that

gold nanoprisms use CTAB as the capping agent in contrast to the citrate capping agent used for the gold nanospheres. This creates a positively charged surface on the gold nanoprisms, which enables the negatively charged DNA to better adsorb onto the gold surface. It would be interesting to see what the ITC data looks for gold nanoprisms, where it seems there should be very specific mechanisms of binding for DNA due to the stacking faults, twin planes, and the presence of iodide ion and cationic surfactant, which can facilitate very specific binding behaviors with DNA. However, it should be noted that the synthesis of the gold nanoprisms should be reliable and reproducible enough to produce monodisperse samples that are stable at a range of pH values. ITC almost always requires that the host will have to be under a different pH than when the nanoparticles are first prepared.

A good compromise between citrate-capped gold nanospheres and CTAB-capped nanoprisms is CTAB-capped gold nanorods. They would still be anisotropic, but the surface charge would be positive like the gold nanoprisms and the synthesis of gold nanorods has been well-established for some time¹³. More studies on the binding affinities of T30 and A30 using ITC could give more reliable insight to the binding of T30 and A30 onto gold nanoprism surfaces.

It would also be interesting and beneficial to see if the change in nanoprism morphology changes using thiolated single stranded DNA, starting with more *ex situ* experiments using TEM and liquid cell STEM. With the covalent bond through the thiol group, there is more sufficient DNA loading and it could help to discern the degree through which the interaction with the DNA bases contributes to the gold nanoparticles

morphology change. Thiolated DNA also should also provide extra stabilization to the gold nanoparticles, regardless of the morphology.

REFERENCES

1. El-Sayed, M. A. *Acc. Chem. Res.* **2001**, *34*, 257-264.
2. Schmid, G. *Chem. Rev.* **1992**, *92*, 1709-1727.
3. Danel, M.-C.; Astruc, D. *Chem. Rev.* **2004**, *104*, 293-346.
4. Murphy, C. J.; Sau, T. K.; Gole, A. M.; Orendorff, C. J.; Gao, J.; Gou, L.; Hunyadi, S. E.; Li, T. *J. Phys. Chem. B* **2005**, *109*, 13857-13870.
5. Zhang, G. *Nanotechnol. Rev.* **2013**, *2*, 269288.
6. Saha, K.; Agasti, S. S.; Kim, C.; Li, X.; Rotello, V. M. *Chem. Rev.* **2012**, *112*, 2739-2779.
7. Boisselier, E.; Astruc, D. *Chem. Soc. Rev.* **2009**, *38*, 1759-1782.
8. Corma, A.; Garcia, G. *Chem. Soc. Rev.* **2008**, *37*, 2096-2126.
9. Jain, P. K.; Lee, K. S.; El-Sayed, I. H.; El-Sayed, M. A. *J. Phys. Chem. B* **2006**, *110*, 7238-7248.
10. Kelly, K. L.; Coronado, E.; Zhao, L. L.; Schatz, G. C. *J. Phys. Chem. B* **2003**, *107*, 668-677.
11. Kooij, E. S.; Ahmed, W.; Hellenthal, C.; Zandvliet, H. J. W.; Poelsema, B. *Colloids Surf., A* **2012**, *413*, 231-238.
12. Li, N.; Zhao, P.; Astruc, D. *Angew. Chem. Int. Ed.* **2014**, *53*, 1756-1789.
13. Jana, N. R.; Gearheart, L.; Murphy, C. J. *J. Phys. Chem. B* **2001**, *105*, 4065-4067.
14. Nikoobakht, B.; El-Sayed, M. *Chem. Mater.* **2003**, *15*, 1957-1962.
15. Wang, C.; Sun, S. *Asian. Chem. J* **2009**, *4*, 1028-1034.
16. Feng, H.; Yang, Y.; You, Y.; Li, G.; Guo, J.; Yu, T.; Shen, Z.; Wu, T.; Xing, B. *Chem. Commun.* **2009**, 1984-1986.
17. Jin, R.; Cao, C. A.; Mirkin, C. A.; Kelly, K. L.; Schatz, G. C.; Zheng, J. G. *Science* **2001**, *294*, 1901-1903.
18. Chen, S.; Carroll, D. L. *Nano Lett.* **2002**, *2*, 1003-1007.
19. Alex, S.; Tiwari, A. *J. Nanosci. and Nanotechnol.* **2015**, *15*, 1869-1894.

20. Alivisatos, A. P.; Johnsson, K. P.; Peng, X.; Wilson, T. E.; Loweth, C. J.; Bruchez, Jr., M. B.; Schultz, P. G. *Nature* **1996**, *382*, 609-611.
21. Mirkin, C. A.; Letsinger, R. L.; Mucic, R. C.; Storhoff, J. J. *Nature* **1996**, *382*, 607-609.
22. Weisbecker, C. S.; Merritt, M. V.; Whitesides, G. M. *Langmuir* **1996**, *12*, 3763-3772.
23. Demers, L. M.; Mirkin, C.; Mucic, R. C.; Reynolds, R. A.; Letsinger, R. L.; Elghanian, R.; Viswanadham, G. *Anal. Chem.* **2000**, *72*, 5535-5541.
24. Herne, T. M.; Michael, T. J. *J. Am. Chem. Soc.* **1997**, *119*, 8916-8920.
25. Wang, Z.; Zhang, J.; Ekman, J. M.; Kenis, P. J. A.; Lu, Y. *Nano Lett.* **2010**, *10*, 1886-1891.
26. Wang, Z.; Tang, L.; Tan, L. H.; Li, J.; Lu, Y. *Angew. Chem.* **2012**, *124*, 9212-9216.
27. Lao, R.; Song, S.; Wu, H.; Wang, L.; Zhang, Z.; He, L.; Fan, C. Electrochemical Interrogation of DNA Monolayers on Gold Surfaces. *Anal. Chem.* **2005**, *77*, 6475-6480.
28. Koo, K. M.; Sina, A. A. I.; Carrascosa, L. G.; Shiddiky, M. J. A.; Trau, M. DNA-bare gold affinity interactions: mechanism and applications in biosensing. *Anal. Methods* **2015**, Advance online publication. doi: 10.1039/C5AY01479D.
29. Li, H. X.; Rothberg, L. J. *JACS* **2004**, *126*, 10958-10961.
30. Li, H. X.; Rothberg, L. J. *Proc. Natl. Acad. Sci. U.S.A.* **2004**, *101*, 14036-14039.
31. Watson, J. D. *The Double Helix: A Personal Account of the Discovery of the Structure of DNA*; Weidenfeld and Nicolson: London, 1968.
32. Nelson, E. M.; Rothberg, L. J. *Langmuir* **2011**, *27*, 1770-1777.
33. Nelson, E. M. *The Adsorption of DNA onto Unmodified Gold Nanoparticles*; PhD Thesis; University of Rochester: Rochester, NY, 2008.
34. Demers, L. M.; Ostblom, M.; Zhang, H.; Jang, N.; Liedberg, B.; Mirkin, C. *JACS* **2002**, *124*, 11248-11249.
35. Ostblom, M.; Liedberg, B.; Demers, L.; Mirkin, C. *J. Phys. Chem. B.* **2005**, *109*, 15150-15160.
36. Jang, N. H. *Bull. Korean Chem. Soc.* **2002**, *23*, 1790-1800.

37. Zheng, H.; Smith, R. K.; Kisielowski, C.; Dahman, U.; Alivisatos, P. *Science* **2009**, *324*, 1309-1312.
38. Liu, Y.; Tai, K.; Dillon, S. J. *Chem. Mater.* **2013**, *25*, 2927-2933.
39. Liao, H. G.; Cui, L. K.; Whitelam, S.; Zheng, H. M. *Science* **2012**, *336*, 1011-1014.
40. Grogan, J. M.; Rotkina, L.; Bau, H. H. *Phys. Rev. E* **2011**, *83*, 061405.
41. Woehl, T. J.; Evans, J. E.; Arslan, L.; Ristenpart, W. D.; Browning, N. D. *ACS Nano* **2012**, *6*, 8599-8610.
42. Woehl, T. J.; Park, C.; James, E. E.; Arslan, I.; Ristenpart, W. D.; Browning, N. B. *Nano Lett.* **2013**, *14*, 373-378.
43. Yuk, J. M.; Park, J.; Ercius, P.; Kim, K.; Hellebusch, D. J.; Crommie, M. F. . L. J. Y. . Z. A. . A. A. P. *Science* **2012**, *336*, 61-64.
44. Parent, L. R.; Robinson, D. B.; Woehl, T. J.; Ristenpart, W. D.; Evans, J. E.; Browning, N. D.; Arslan, I. *ACS Nano* **2012**, *6*, 3589-3596.
45. De Yoreo, J. *Nature Mater.* **2013**, *12*, 284-285.
46. de Jonge, N.; Poirier-Demers, N.; Demers, H.; Peckys, D. B.; Drouin, D. *Ultramicroscopy* **2010**, *110*, 1114-1119.
47. Klein, K. L.; Anderson, I. M.; de Jonge, N. *J. Microscopy* **2011**, *242*, 117-123.
48. Ring, E. A.; de Jonge, N. *Microsc. Microanal.* **2010**, *16*, 622-629.
49. Swallow, A. J., Ed. *Radiation Chemistry: An Introduction*; Wiley Press: New York, 1973.
50. Millstone, J. E.; Wei, W.; Jones, M. R.; Yoo, H.; Mirkin, C. A. *Nano Lett.* **2008**, *8*, 2526-2529.
51. Lofton, C.; Sigmund, W. *Adv. Funct. Mater.* **2005**, *15*, 1197-1208.
52. Millstone, J. E.; Metraux, G. S.; Mirkin, C. A. *Adv. Funct. Mater.* **2006**, *16*, 1209-1214.
53. Millstone, J. E. *Synthesis, Properties, and Applications of Colloidal Gold Nanoprisms*; Northwestern University: Evanston, IL, 2008.
54. Wang, Z. L.; Gao, R. P.; Nikoobakht, B.; El-Sayed, M. A. *J. Phys. Chem. B* **2000**, *104*, 5417-5420.

55. Zeng, J.; Xia, X.; Rycenga, M.; Hanneghan, P.; Qingge, L.; Xia, Y. *Angew. Chemie.* **2011**, *123*, 258–2263.
56. Millstone, J. E.; Hurst, S. J.; Metraux, G. S.; Cutler, J. I.; Mirkin, C. A. *Small* **2009**, *6*, 646-664.
57. Storhoff, J. J.; Elghanian, R.; Mirkin, C. A.; Letsinger, R. E. *Langmuir* **2002**, *18*, 6666-6670.
58. Rudolph, R.; Jungjohann, K. L.; Wheeler, D. R.; Brozik, S. M. *Microsc. Microanal.* **2014**, *20*, 437-444.
59. Kimura-Suda, H.; Petrovykh, D. Y.; Tarlov, M. J.; Whitman, L. J. *JACS* **2003**, *125*, 9014-9015.
60. Opdahl, A.; Petrovykh, D. Y.; Kimura-Suda, H.; Tarlov, M. J.; Whitman, L. J.; \. *PNAS* **2007**, *104*, 9-14.
61. Grabar, K. C.; Freeman, R. G.; Hommer, M. B.; Natan, M. J. *Anal. Chem.* **1995**, *67*, 735-743.
62. Evan, J. E.; Junjohann, K. L.; Browning, N. D.; Arslan, I. *Nano Lett.* **2011**, *11*, 2809-2813.
63. Zhang, X.; Servos, M. R.; Liu, J. *Langmuir* **2012**, 3896-3902.
64. Faraday, M. *Phil. Trans. R. Soc. Lond.* **1857**, *147*, 145-181.
65. Perez-Juste, J.; Liz-Marzan, L. M.; Carnie, S.; Chan, D. Y. C.; Mulvaney, P. *Adv. Funct. Mat.* **2004**, *14*, 571-579.
66. Williamson, M. J.; Tromp, R. M.; Vereecken, P. M.; Hull, R.; Ross, F. M. *Nat. Mater.* **2003**, *2*, 532-536.
67. Li, D. S.; Nielsen, M. H.; Lee, J. R. I.; Frandsen, C.; Banfield, J. F.; De Yoreo, J. J. *Science* **2012**, *336*, 1014-1018.
68. Gourishankar, A.; Shukla, S.; Ganest, K. N.; Sastry, M. *JACS* **2004**, *126*, 13186-13187.
69. Nellist, P. D.; Pennycook, S. J. *Advances in Imaging and Electron Physics* **2000**, *123*, 173-206.